https://doi.org/10.3311/PPee.42515

Periodica Polytechnica Electrical Engineering and Computer Science

Engineering and Electrical Behavior of Au/CuI/$CsGeI_3$/$CsSnI_3$/ZnSe/FTO Perovskite Solar Cells: Numerical Studies by Scaps and DFT

Keltoum Dris[1], Soufyane Belhachi[2,3], Mostefa Benhaliliba[1*], Charazade-Elj Benouis[1], Hiba Bouandas[4], Rajeev Kumar[5]

[1] Film Device Fabrication-Characterization and Application FDFCA Research Group USTOMB, 31130, Oran, Algeria
[2] Artificial Intelligence Laboratory for Mechanical and Civil Structures, and Soil, University of Salhi Ahmed, Naama, P.O. Box 66, Naama, 45000, Algeria
[3] Faculty of Technology, University of Salhi Ahmed, Naama, P.O. Box 66, Naama, 45000, Algeria
[4] Applied Optics Laboratory, Institute of Optics and Precision Mechanics, University Setif 1, 19000 Setif, Algeria
[5] Department of Electronics and Communication, Engineering, Graphic Era (Deemed to Be University), Dehradun, Uttarakhand 248001, India
[*] Corresponding author, e-mail: mostefa.benhaliliba@univ–usto.dz

Received: 15 October 2025, Accepted: 11 December 2025, Published online: 17 January 2026

Abstract

This study evaluates the potential of the lead-free double perovskites $CsGeI_3$ and $CsSnI_3$ for high-performance photovoltaic applications through a combined approach integrating SCAPS–1D solar cell modeling with density functional theory (DFT). Using the Au/CuI/$CsGeI_3$/$CsSnI_3$/ZnSe/FTO device configuration, SCAPS–1D simulations identified optimal absorber-layer parameters, including thicknesses of 1000 nm for $CsGeI_3$ and 700 nm for $CsSnI_3$, a doping level of 10^{19} cm^{-3}, and a defect density of 10^{14} cm^{-3}. Under these optimized conditions, the device achieved high performance, delivering a Voc of 1.17534 V, Jsc of 30.54 $mA \cdot cm^{-2}$ FF of 88.08%, and a PCE of 31.61%. To complement these device-level results, DFT calculations were performed to examine the structural, mechanical, thermodynamic, and electronic characteristics of both materials. The optimized lattice parameters, elastic constants, and derived mechanical moduli confirmed structural integrity and ductile behavior, while the calculated sound velocities and Debye temperatures supported their thermal stability. Electronic-structure analyses revealed narrow mBJ band gaps of 0.71 eV for $CsGeI_3$ and 0.69 eV for $CsSnI_3$, indicating strong absorption capabilities across the visible-NIR region. This work presents the first application of a $CsGeI_3$-$CsSnI_3$ dual-absorber solar cell, offering a promising strategy for improving light absorption, carrier transport, and overall device performance. Furthermore, these combined results demonstrate that $CsGeI_3$ and $CsSnI_3$ possess favorable optoelectronic properties and high simulated photovoltaic efficiency, making them excellent candidates for future eco-friendly solar-energy technologies.

Keywords

$CsGeI_3$, $CsSnI_3$, perovskites, density functional theory, elastic properties, mechanical properties, photovoltaic applications, optoelectronic devices, GGA–mBJ, SCAPS–1D

1 Introduction

Current research on perovskite solar cells (PSCs) faces a major challenge: developing devices that are both efficient, stable, and lead-free, in order to meet environmental requirements while maintaining high energy conversion efficiency. In particular, the combination of inorganic perovskite compounds in a dual-absorber configuration remains poorly explored, despite the potential synergy between materials with complementary properties. The main objective of this study is therefore to identify and optimize a lead-free perovskite combination capable of enhancing photovoltaic conversion while ensuring high thermal and chemical stability. In recent years, PSCs have achieved remarkable progress, attracting strong scientific interest due to their rapid efficiency improvement, increasing from 3.8% to 25.7% within a decade [1–3]. This improvement is mainly attributed to the exceptional optoelectronic properties of halide perovskites, including high absorption coefficients, low exciton binding energies, long carrier diffusion lengths, ideal band gaps, and high carrier mobilities [2–5]. Their tunable

Cite this article as: Dris, K., Belhachi, S., Benhaliliba, M., Benouis, C. E., Bouandas, H., Kumar, R. "Engineering and Electrical Behavior of Au/CuI/$CsGeI_3$/$CsSnI_3$/ZnSe/FTO Perovskite Solar Cells: Numerical Studies by Scaps and DFT", Periodica Polytechnica Electrical Engineering and Computer Science, 2026. https://doi.org/10.3311/PPee.42515

band gaps, wide absorption range, low effective carrier masses, and abundant point defects further enhance their potential for photovoltaic and optoelectronic applications [6–13]. Several studies have investigated $CsGeI_3$ or $CsSnI_3$ as a single absorbing layer in perovskite solar cells. For example, Asfandyar Ali Khan et al. employed a PSC structure of the type $CMTS/CsGeI_3/CdZnS$ based solely on $CsGeI_3$ and achieved an efficiency of 25% [14]. Similarly, Anas Ahmad et al. analyzed three structures using $CsSnI_3$; among them, the $GO/CsSnI_3/CeO_2$ configuration exhibited the highest PCE (21.52%), followed by $GO/CsSnI_3/WO_3$ (21.4%) and $MoS_2/CsSnI_3/WO_3$ (15.64%) [15]. However, none of these works examined the simultaneous use of $CsGeI_3$ and $CsSnI_3$ within the same solar cell, which represents the main originality of the present study. In this context, combining $CsGeI_3$ and $CsSnI_3$ in a dual-absorber architecture appears to be a promising approach to enhance light absorption, optimize charge-carrier transport, and reduce recombination losses. Such a configuration has the potential to achieve higher efficiency than structures based on a single active layer.

Similarly, several other studies are found on Cs-based perovskites [13, 16–23], using generalized gradient approximation methods, the study of Aneer et al. [24] investigates the impact of cation and anion substitutions under isosymmetric compression. The results reveal how these substitutions influence the perovskites' properties. Un-Gi et al. [25] conducted a detailed investigation into the thermoelectric properties of cubic $CsBI_3$ (B = Pb, Sn, Ge) perovskites at 700 K, utilizing first-principles lattice dynamics, anharmonic phonon renormalization, and the Boltzmann transport equation. Their study revealed that these materials exhibit extremely low lattice thermal conductivities (<0.6 W/mK^2) and substantial thermopower factors (>1.5 mW/mK^2). Notably, $CsGeI_3$ and $CsSnI_3$ showed ZT values exceeding 0.95 when *n*-type doping was applied, underscoring their potential as efficient, low-cost thermoelectric materials. In another study, Md et al. [26] explored lead-free cubic perovskites $CsBX_3$ (B = Sn, Ge; X = I, Br, Cl) for solar cell applications, examining their structural, electronic, optical, and mechanical characteristics using Density Functional Theory (DFT). The results showed these materials are stable, with high optical absorption, low reflectivity, and strong optical conductivity, especially in the Ge-based compounds, indicating their promise for photovoltaic use which outperforms Pb-based alternatives. Among the materials, $CsGeI_3$ and $CsGe(I_{0.7}Br_{0.3})_3$ show the highest potential for solar cell applications, with the latter offering improved mechanical ductility.

Furthermore, the findings of Khalil et al. [27] indicate metallic behavior due to a lack of a bandgap, with lattice constants determined using both PBE-GG and LDA functionals. $FrGaH_3$ shows promise for hydrogen storage, achieving a gravimetric capacity of 2.1 wt%, while all compounds exhibit antiferromagnetic properties and minimal energy loss with high conductivity. The study of Noor et al. [28] explores the potential of double perovskite halides A_2ScInI_6 (A = Rb, Cs) for renewable energy applications, analyzing their structural, electronic, and optical properties using FP − LAPW + lo DFT methods. Results confirm their stability, ductility, and infrared light absorption, making them suitable for optoelectronic devices. Additionally, transport properties like electrical and thermal conductivity, Seebeck coefficient, and figure of merit suggest promising thermoelectricperformance, supporting their use in energy-related technologies. Earlier research has demonstrated that all-inorganic perovskite $CsSnI_3$ can be produced via a melting-solidification process, with a high melting point of 451 °C, highlighting its remarkable inherent thermal stability [29, 30]. In contrast, organic-inorganic hybrids like $MASnI_3$ and $FASnI_3$ begin to break down at temperatures around 200 °C, showcasing their relatively lower thermal durability [31].

The reviewed studies collectively advance sustainable hydrogen production, CO_2 management, and LNG liquefaction by integrating renewable energy, waste-heat recovery, and advanced thermodynamic cycles. Works [32–34] achieved major reductions in hydrogen liquefaction energy demand, lowering SPC to 4.32–6.60 kWh kg^{-1} LH_2 with efficiencies up to 65%. Studies [35, 36] further improved performance through liquid-air energy recovery and cascade He/H_2 refrigeration, reaching SEC values near 5.96 kWh kg^{-1} LH_2 and SOFC efficiencies exceeding 62%, with economically attractive payback periods (~4.25 years). Research [37, 38] enhanced solar-energy utilization and CO_2 capture/liquefaction, reporting liquid CO_2 production of 2.641 kg s^{-1} and COP values of 3.66. Additional contributions in [39] demonstrated high-output CO_2 liquefaction (9307 kmol h^{-1}) and exergy efficiencies up to 58.48% using load-shifting and geothermal-ORC integration. Finally, study [40] optimized solar-assisted LNG liquefaction, achieving a COP of 3.20, SEC of 0.229 kWh kg^{-1} LNG, and exergy efficiency of 42.77%. Overall, these works highlight how hybrid renewable-wasteheat systems significantly improve efficiency and economic viability in clean energy technologies. In this study, we explore the physical properties of $CsGeI_3$ and $CsSnI_3$ using advanced computational techniques to provide a clear and focused understanding of their potential in modern energy technologies. Unlike previous works that examined these materials separately, our study presents a combined, systematic investigation integrating density functional theory (DFT) calculations with SCAPS-1D photovoltaic simulations, offering a more comprehensive assessment of their performance in the same device architecture. This dual-method approach enables us to correlate intrinsic material characteristics – such as structural stability, mechanical behavior, electronic band features, and optical response – with devicelevel efficiency. By addressing existing gaps in the literature and highlighting the advantages of lead-free perovskites, our work brings forward new insights, methodological clarity, and practical value for the design of next-generation environmentally friendly solar cells.

2 Computational details

This research was conducted using the SCAPS-1D simulator, a numerical tool specifically designed for modeling thin-film heterojunction solar cells. Developed by Marc Burgelman and his team at Ghent University in Belgium, SCAPS is built on the LabWindiws/CVI platform by National Instruments. Since its introduction at the 2nd World Conference on Photovoltaic Solar Energy Conversion in 1998, it has been made available to selected research institutions specializing in photovoltaics. SCAPS-1D solves the fundamental semiconductor transport and continuity equations across multiple layers, accounting for position-dependent doping profiles and energy band distributions under various illumination conditions. The simulation involves iterative processes that continue until the algorithm reaches convergence. Originally intended for the $CuInSe_2$ and CdTe families of solar cells, SCAPS has since been upgraded to include the simulation of crystalline solar cells (such as Si and GaAs) as well as amorphous cells (like *a*-Si and Si micromorphs) [41, 42]. Fig. 1 illustrates the solar cell configuration of $Au/CuI/CsGeI_3/CsSnI_3/ZnSe/FTO$, as well as the energy band alignment simulated using the SCAPS tool. By investigating this configuration, we examine its efficiency and performance, which could inform the development of high-efficiency, environmentally friendly photovoltaic devices. This software enables the modeling of solar cells with up to seven distinct layers, each defined by specific characteristics such as doping profiles, thickness, energy levels at donor or acceptor sites, and light absorption. It computes parameters including charge concentrations, energy band structure, currents, and current-voltage (J–V) characteristics. The material properties and spectral response are derived through solutions to three fundamental equations, starting with the Poisson equation [43]:

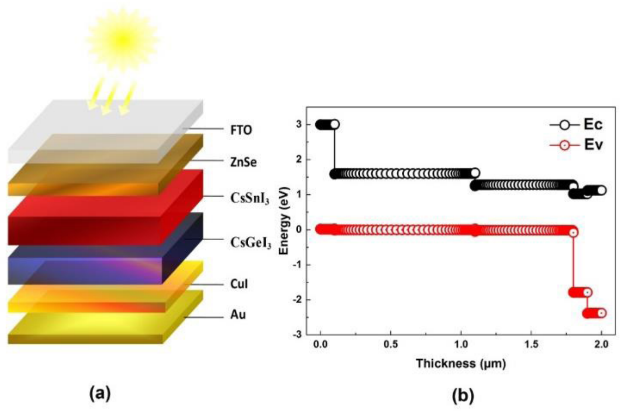

Fig. 1 (a) Structure of the $Au/CuI/CsGeI_3/CsSnI_3/ZnSe/FTO$ solar cell, (b) energy band alignment

$$-\partial/\partial x\left[-\varepsilon(x)\partial V/\partial x\right] = q\left[p(x)-n(x)+N_D^+(x)-N_A^-(x)+p_t(x)-n_t(x)\right] \quad (1)$$

The hole continuity equation [44]:

$$\partial P/\partial t = 1/q\left(\partial J_p\right)/\partial x + G_p - R_p \quad (2)$$

The electron continuity equation [44] :

$$\partial n/\partial t = 1/q\left(\partial J_n\right)/\partial x + G_n - R_n \quad (3)$$

With: q is the charge; V is the potential; ε is dielectric permeability n is concentration offree electrons; p is concentration of free holes; $N_A^-(x)$ is the concentration of ionized acceptors; $N_A^-(x)$ is the concentration of ionized donors; G_p is the hole generation rate; G_n is the rate of generation of electrons; $n_t(x)$ is the density of trapped electrons; $p_t(x)$ is the density of trapped holes; R_p is the recombination rate of holes; R_n is the recombination rate of electrons; J_p is the current density of the hole; J_n is the current density of the electron. The simulations were conducted with SCAPS-1D version 3.3.07, using the input parameters listed in Tables 1 and 2 [40, 43, 45, 46] and applying standard test conditions: AM1.5G solar spectrum, a temperature of 300 K, and a power density of

Table 1 Properties of the materials (CuI, $CsGeI_3$, $CsSnI_3$, ZnSe and FTO) utilized in cell simulation

Parameters	CuI (*p*-type) [24]	$CsGeI_3$ (*p*-type)	$CsSnI_3$ (*p*-type)	ZnSe (*n*-type)	FTO (*n*-type)
Thickness (nm)	100	400	400	100	100
Band gap (eV)	2.98	1.6	1.3	3.3	3.5
Electron affinity (eV)	2.1	3.52	3.9	4.1	4.0
Dielectric permittivity	6.5	18.0	18	9.0	9.0
CB effective density of states (cm^{-3})	2.8×10^{19}	1.0×10^{18}	2.2×10^{17}	4×10^{18}	2.2×10^{18}
VB effective density of states (cm^{-3})	1.1×10^{19}	1.0×10^{19}	1.8×10^{19}	1.0×10^{19}	1.8×10^{19}
Electron thermal velocity ($cm\ s^{-1}$)	1.0×10^{7}	1.0×10^{7}	1.0×10^{7}	1.0×10^{7}	1.0×10^{7}
Hole thermal velocity ($cm\ s^{-1}$)	1.0×10^{7}	1.0×10^{7}	1.0×10^{7}	1.0×10^{7}	1.0×10^{7}
Electron mobility ($cm^2\ V^{-1}\ s^{-1}$)	100	20	0.2	100	20
Hole mobility ($cm^2\ V^{-1}\ s^{-1}$)	43.9	20	0.2	25	10
Shallow uniform donor density ND (cm^{-3})	0	0	0	1.0×10^{20}	2×10^{19}
Shallow uniform acceptor density NA (cm^{-3})	2.0×10^{19}	2.0×10^{16}	2.0×10^{18}	0	0
Nt (cm^{-3}) total	1.0×10^{15}	1.0×10^{15}	1.0×10^{14}	1.0×10^{15}	1.0×10^{16}
Reference					

Table 2 The input properties for the CuI/; /and /ZnSe interfaces

Interface layer	CuI/$CsGeI_3$	$CsGeI_3$/$CsSnI_3$	$CsSnI_3$/ZnSe
Type of defect	neutral	neutral	neutral
Electrons capture cross-section (cm^2)	1.0×10^{19}	1.0×10^{19}	1.0×10^{19}
Hole capture cross-section (cm^2)	1.0×10^{19}	1.0×10^{19}	1.0×10^{19}
Energy distribution	single	single	Single
Defect energy level reference (E_t)	above the highest EV	above the highest EV	above the highest EV
Energy level related to reference (eV)	0.6	0.6	0.6
Total density (integrated over all energies) (cm^{-2})	1.0×10^{10}	1.0×10^{10}	1.0×10^{10}

(1000 W m^{-2}) [47]. In this study, we also conducted a detailed analysis of the structural, electronic, optical, elastic, and mechanical properties of $CsGeI_3$ and $CsSnI_3$ using the WIEN2k [48] based on the full-potential linearized augmented plane wave (FP–LAPW) approach under the framework of density functional theory (DFT) [49].

Structural optimizations, including lattice parameters and atomic positions, were performed using the Perdew-Burke-Ernzerhof (PBE) exchange-correlation functional within the generalized gradient approximation (GGA) [50]. To achieve accurate electronic structure calculations, the modified Becke-Johnson (mBJ) potential [51] was employed, which is known for improving band gap predictions for semiconductor materials such as $CsGeI_3$ and $CsSnI_3$. The parameters used in this study included a plane-wave cutoff RmtKmax = 7 and Gmax = 16 Ry, chosen to ensure sufficient convergence. Muffin-tin radii (Rmt) were set to 2.5 atomic units (a.u.) for Cs, 2.2 a.u. for Ge and Sn, and 2.0 a.u. for I, to fit the atomic sizes into the crystal structure. For accurate integration in reciprocal space, a dense k-point grid of 10 × 10 × 10 was used for Brillouin zone sampling [45, 52]. The optical properties such as absorption, refractive index, and extinction coefficient were derived from the dielectric function, showing strong potential for $CsGeI_3$ and $CsSnI_3$ in photovoltaic applications. Additionally, the thermal stability of these materials was explored to evaluate their feasibility for use in practical energy systems.

3 Results and discussion

3.1 SCAPS 1D simulation study

3.1.1 Optimization of $CsGeI_3$ and $CsSnI_3$ thickness

Optimizing the thickness of active layers in perovskite solar cells is crucial for maximizing energy conversion efficiency. The active layers, particularly those made of perovskite, play a key role in light absorption and charge carrier generation (electrons and holes), which contributes to the production of electric current. An appropriate thickness ensures maximum light absorption while minimizing recombination losses, which could otherwise reduce cell efficiency [53]. Several studies have focused on optimizing the thickness of various perovskite absorber layers, demonstrating that precise thickness adjustments can significantly enhance key photovoltaic parameters, such as open-circuit voltage (Voc), short-circuit current (Jsc), fill factor (FF), and power conversion efficiency (PCE) [54–56].

In this study, we explored the impact of $CsGeI_3$ and $CsSnI_3$ layer thicknesses on solar cell performance to determine the optimal thicknesses for maximizing the cell's overall energy efficiency. The results obtained are represented in the contour maps Fig. 2(a)-(d), each illustrating the relationship between layer thickness and photovoltaic performance.

Contour map (Fig. 2(a)): This map shows the variation of Voc with the thickness of the absorber layers. Voc generally decreases as the thickness of the layers increases. However, the optimal thicknesses of 1000 nm for $CsGeI_3$ and 700 nm for $CsSnI_3$ lead to a Voc of 1.01065 V. These values were chosen as they strike a balance between maximum light absorption and minimal recombination losses. With these optimized thicknesses, the generated charge carriers reach the electrodes more quickly, reducing non-radiative recombination and enhancing overall cell performance.

Contour map (Fig. 2(b)): This map shows the variation of Jsc with thickness. As the thickness of the absorbing layers increases, Jsc initially increases due to enhanced light absorption, but it stabilizes beyond the optimal thickness. For the chosen optimal thicknesses (1000 nm for $CsGeI_3$ and 700 nm for $CsSnI_3$), a Jsc of 33.9614 mA cm^{-2} is achieved. The initial increase in Jsc is due to the greater number of electron-hole pairs generated in thicker layers. However, beyond these optimal thicknesses, Jsc plateaus, suggesting that charge carrier collection is maximized, and excess recombination losses do not significantly increase.

Contour map (Fig. 2(c): This map shows the variation of the fill factor (FF) with layer thickness. The FF remains relatively stable across a broad range of thicknesses, although it decreases slightly with greater thickness. At the optimal thicknesses (1000 nm for $CsGeI_3$ and 700 nm for $CsSnI_3$), an FF of 81.6793% is achieved. This stability indicates effective management of parasitic resistances, and the observed decrease in FF with increasing thickness is minimal, suggesting that the increased thickness does not significantly affect the cell's internal resistance. As a result, the device maintains optimal performance [57, 58].

Contour map (Fig. 2(d)): This map illustrates the power conversion efficiency (PCE) as a function of the absorber layer thickness. The PCE reaches its maximum at the optimized thicknesses of 1000 nm for $CsGeI_3$ and 700 nm for $CsSnI_3$, resulting in a PCE of 28.0348%. This optimal efficiency is achieved by balancing high light absorption with minimized recombination losses. The chosen thicknesses ensure that enough light is absorbed to generate a large number of charge carriers, without excessively increasing the probability of recombination, thereby maximizing the cell's overall efficiency.

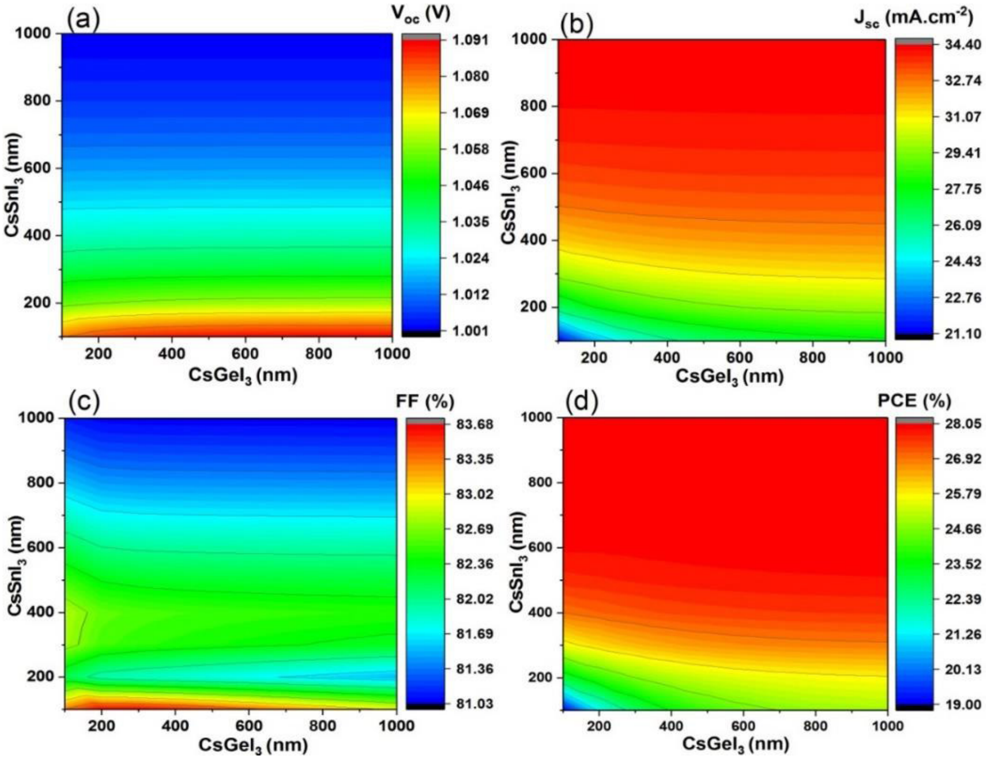

Fig. 2 Contour maps showing the variation of photovoltaic parameters with $CsGeI_3$ and $CsSnI_3$ thicknesses: (a) Voc (V), (b) Jsc (mA.cm^{-2}), (c) FF (%), and (d) PCE (%)

Fig. 3 presents Nyquist diagrams for different thicknesses of $CsGeI_3$ with a fixed $CsSnI_3$ thickness of 700 nm. The results show an increase in impedance (−Z″) with $CsGeI_3$ thickness, reaching a peak and then decreasing. The initial increase in −Z″ reflects the accumulation of charge carriers and elevated series resistance within thicker absorber layers, which hinder efficient charge transport and lead to higher recombination losses. This is consistent with the formation of more trap states and longer carrier diffusion paths that elevate the recombination probability.

As the thickness increases further, the impedance begins to decline, indicating a shift where excessive thickness no longer contributes meaningfully to recombination or resistive buildup, possibly due to saturation effects or improved bulk transport. At the optimal thickness of 1000 nm for $CsGeI_3$, the impedance reaches a balance point where charge extraction is efficient and recombination losses are minimized, thus correlating directly with improved photovoltaic performance [59].

The optimal thicknesses of 1000 nm for $CsGeI_3$ and 700 nm for $CsSnI_3$ allow the solar cell to achieve maximum performance, with a Voc of 1.01065 V, a Jsc of 33.9614 mA.cm^{-2}, an FF of 81.6793%, and a PCE of 28.0348%. These results highlight the importance of optimizing the thickness of absorbing layers to maximize light absorption while controlling recombination and transport losses. This work aligns with similar studies that have investigated analogous parameters and achieved high efficiencies by optimizing the $CsSnI_3$ absorber thickness through simulations, underscoring the impact of absorber thickness and resistance minimization on performance [60, 61].

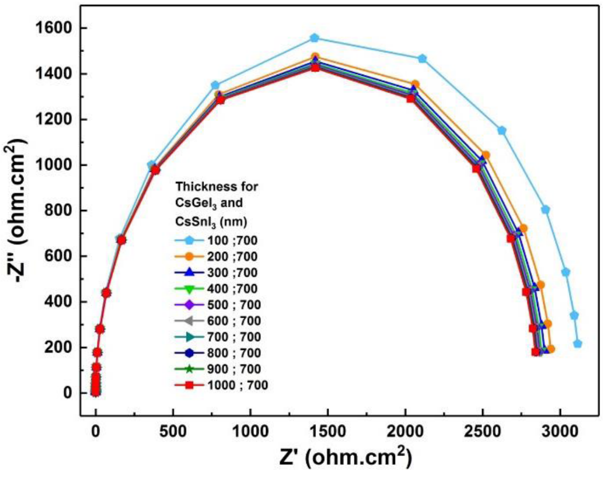

Fig. 3 Nyquist plot illustrating the evolution of impedance as a function of absorber thickness

3.1.2 Optimization of $CsGeI_3$ and $CsSnI_3$ doping density

Optimizing the doping density in perovskite solar cells is a key strategy for enhancing their overall performance and power conversion efficiency. Numerous studies have shown that tuning the doping levels within the absorber layers can significantly impact critical photovoltaic parameters, including the open-circuit voltage (Voc), short-circuit current density (Jsc), fill factor (FF), and power conversion efficiency (PCE). A clear understanding of the relationship between doping density and device performance is essential for the development of high- efficiency solar cells and for mitigating the limitations associated with recombination losses [62, 63]. In this study, the impact of doping density in the absorbing layers $CsGeI_3$ and $CsSnI_3$ on solar cell performance was examined. The results reveal significant trends in key performance parameters: Voc, Jsc, FF, and PCE, as shown in the contour maps of Fig. 4, ranging from Fig. 4(a) to Fig. 4(d).

Contour map in Fig. 4(a) shows that varying the doping density reveals a complex relationship with solar cell performance metrics. For $CsGeI_3$, the Voc remained relatively stable at around 1.003 V across the different doping densities, indicating that the increase in doping did not adversely affect the voltage output. However, the most notable improvements were observed in Jsc, FF, and PCE as the doping density of $CsSnI_3$ was increased. Contour map in Fig. 4(b) indicates that the short-circuit current density (Jsc) also followed a positive trend, reaching a maximum of 34.05 mA.cm^{-2} at the highest doping level. This increase reflects a direct consequence of enhanced light absorption and the generation of more electron-hole pairs, which are critical for achieving higher current output.

Contour map in Fig. 4(c) reveals that the fill factor (FF) showed a progressive increase, peaking at 88.08% with a doping density of 10^{19} cm^{-3}. This increase suggests better management of series and shunt resistances, likely due to more favorable carrier mobility at optimal doping levels. Higher doping concentrations may facilitate effective charge transport, reducing recombination losses and allowing for a more efficient collection of generated carriers. Contour map in Fig. 4(d) indicates that at lower doping levels (10^{11} cm^{-3}), the PCE was approximately 24.11%, which gradually increased with higher doping concentrations. Notably, at a doping level of 10^{19} cm^{-3}, the PCE peaked at 31.61%. This enhancement can be attributed to improved charge carrier concentration leading to increased light absorption and enhanced collection efficiency of charge carriers [64, 65]. These results underscore the

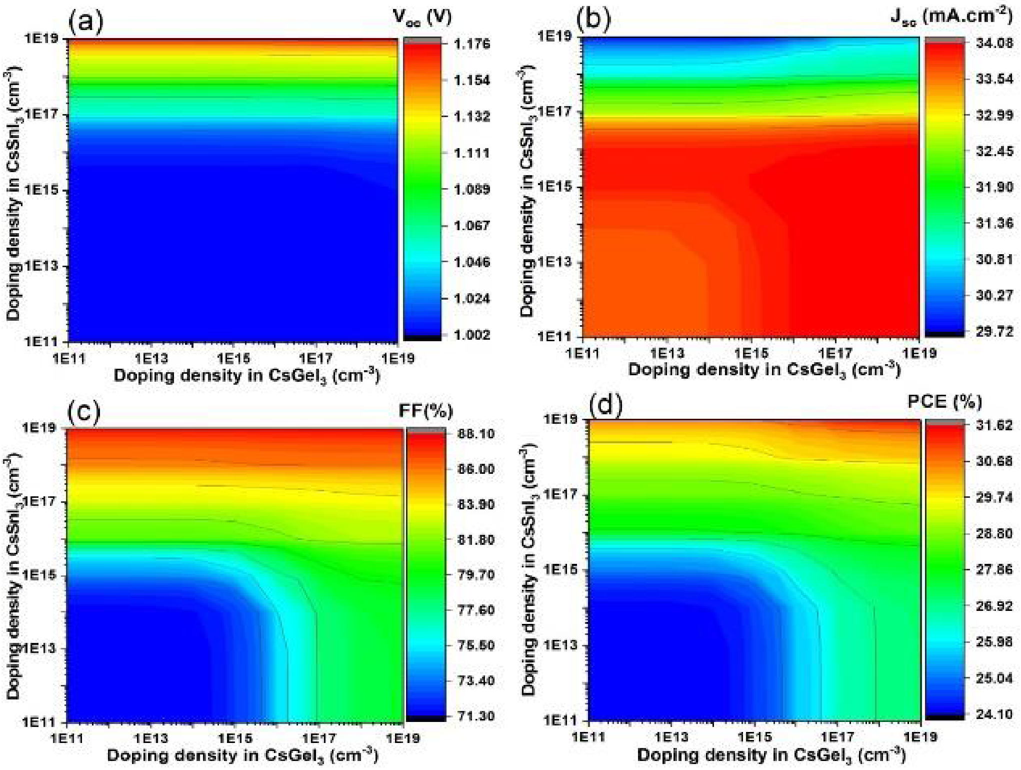

Fig. 4 Contour maps showing the variation of photovoltaic parameters with CsGeI$_3$ and CsSnI$_3$ doping density: (a) Voc (V), (b) Jsc (mA.cm^{-2}), (c) FF (%), and (d) PCE (%)

significant role of doping density in optimizing the performance of perovskite solar cells. The findings indicate that while maintaining a stable Voc, increased doping densities in CsSnI$_3$ substantially improve Jsc, FF, and PCE, demonstrating the importance of tuning doping levels to enhance solar cell efficiency. A doping density of 10^{19} cm^{-3} was chosen as optimal for the CsGeI$_3$ and CsSnI$_3$ layers, corresponding to a Voc of 1.17533 V, a Jsc of 30.5308 mA cm^{-2}, a FF of 88.0836%, and an efficiency of 31.6076%.

These results are in good agreement with the findings of Tariq et al., who investigated the impact of doping concentration on the performance of lead-free perovskite solar cells. Their study highlighted the critical role of doping density in enhancing solar cell efficiency, with a specific focus on key photovoltaic parameters.

Through numerical modeling of a germanium (Ge)-based solar cell structure, they initially achieved a power conversion efficiency (PCE) of 17.74%. By optimizing the doping concentration and employing copper-based hole transport materials, the efficiency was further improved, reaching up to 23.56% [53].

3.1.3 Optimization of CsGeI$_3$ and CsSnI$_3$ defect density

Optimizing the defect density in perovskite solar cells is essential for enhancing their performance and overall power conversion efficiency. Numerous studies have shown that variations in defect densities within the absorbing layers can significantly influence key parameters such as open-circuit voltage (Voc), short-circuit current density (Jsc), fill factor (FF), and power conversion efficiency (PCE) [55, 57]. Understanding the relationship between defect density and solar cell performance is essential for developing high-efficiency devices and overcoming limitations posed by recombination losses.

In this study, the impact of defect density in the absorbing layers CsGeI$_3$ and CsSnI$_3$ on solar cell performance was examined. The results reveal significant trends in key performance parameters: Voc, Jsc, FF, and PCE, as shown in the contour maps in Fig. 5, ranging from Fig. 5(a) to Fig. 5(d). The contour map in Fig. 5(a) shows that the variation of defect density reveals a complex relationship with the performance metrics of the solar cells. For CsGeI$_3$, the Voc remained relatively stable at around 1.175 V across the different defect densities, indicating that the increase in defect density did not have a detrimental effect on the output voltage. However, the most notable improvements were observed in Jsc, FF, and PCE as the defect density of CsSnI$_3$ increased [59]. The contour map in Fig. 5(b) indicates that at lower defect densities (10^{14} cm^{-3}), the PCE was approximately 31.61%, which gradually decreased

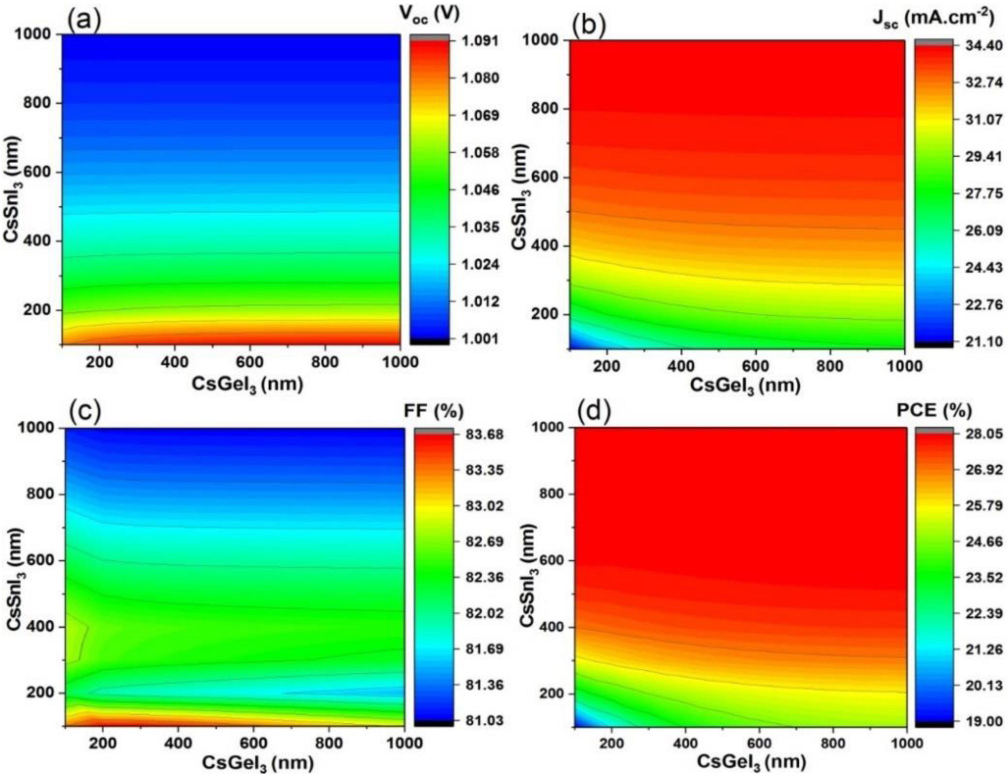

Fig. 5 Contour mapping of PV parameters for $CsGeI_3$ and $CsSnI_3$ defect density: (a) Voc (V), (b) Jsc ($mA.cm^{-2}$), (c) FF (%), and (d) PCE (%)

with higher defect densities. Notably, at a defect density of 10^{19} cm^{-3}, the PCE dropped to 1.22%. This decline can be attributed to increased recombination losses, resulting in a reduced concentration of charge carriers and therefore lower light absorption [59].

The contour map in Fig. 5(c) reveals that the fill factor (FF) showed a progressive decrease, reaching a maximum of 88.08% with a defect density of 10^{14} cm^{-3}. This decrease suggests that higher defect densities negatively affect the management of series and shunt resistances, likely due to reduced carrier mobility [62, 66].

The contour map in Fig. 5(d) indicates that the short-circuit current density (Jsc) decreases with increasing defect density. A value of 30.54 mA cm^{-2} was obtained at the lowest defect density (10^{14} cm^{-3}).

This decrease is directly due to increased defect-induced recombination losses, which reduce the number of photogenerated electron-hole pairs contributing to the output current [63, 67]. These results underscore the significant role of defect density in optimizing the performance of perovskite solar cells, as illustrated in Fig. 6.

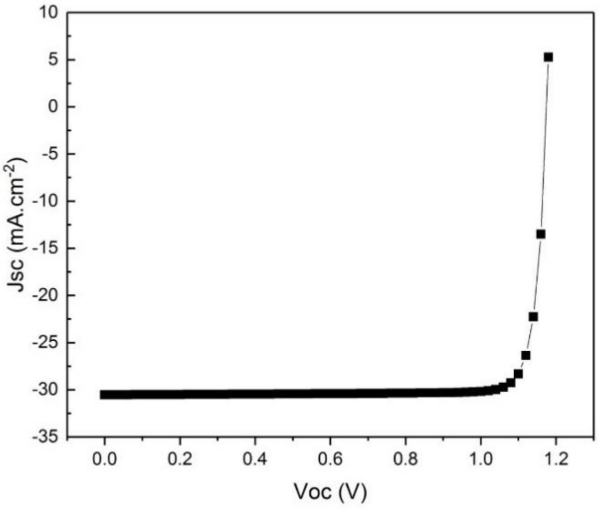

Fig. 6 J-V characteristics of the optimized cell

The findings indicate that while maintaining a relatively stable Voc, increased defect densities in $CsSnI_3$ significantly reduce Jsc, FF, and PCE, demonstrating the importance of minimizing defect levels to enhance solar cell efficiency. A defect density of 10^{14} cm^{-3} has been chosen as the optimal defect density for these two layers, corresponding to the following parameters: Voc (V) = 1.17354, Jsc (mA cm^{-2}) = 30.53567, FF (%) = 88.0837, PCE (%) = 31.613

3.2 DFT investigation

3.2.1 Structural robustness, along with elastic, mechanical, and thermodynamic properties

Structural Robustness

The compounds $CsBI_3$ (where B = Sn, Ge) adopt a cubic crystal structure that aligns with the space group Pm3m (no. 221). In this arrangement, each unit cell contains a total of five atoms, representing a single formula unit of the compound. Here, Cs atoms are located at the corners of the cube, assigned to the 1a Wyckoff position with fractional coordinates (0, 0, 0). Meanwhile, the B atom is centrally positioned in the unit cell providing structural stability, associated with the 1b Wyckoff site and coordinates (1/2, 1/2, 1/2), establishing the central point of the cubic framework. The halide atoms (X) are distributed at the face centers, occupying the 3c Wyckoff sites with fractional coordinates (0, 1/2, 1/2). This spatial arrangement results in a three-dimensional network where each B atom is octahedrally coordinated by X atoms, forming a robust [BX_3] octahedron and imparting structural stability to the perovskite lattice. The stability of these compounds is further supported by analyzing the total energy as a function of volume, as illustrated in Fig. 7. The Murnaghan EOS was utilized for the mechanical optimization in this investigation [64]. For both materials, the curves exhibit a minimum point corresponding to the equilibrium volume, where the system is most stable. $CsGeI_3$ achieves its minimum energy at a smaller volume compared to $CsSnI_3$, reflecting the smaller atomic size of Ge relative to Sn. The well-shaped parabolic curves signify the mechanical stability of both materials, ensuring that they can withstand small deformations without experiencing significant energy changes. For $CsGeI_3$, the optimized lattice constant is 6.0075 Å, while for $CsSnI_3$ it is slightly larger at 6.2994 Å, as seen from the calculated data in Table 3 [68–74].

This difference in lattice constants is primarily attributed to the larger atomic radius of Sn compared to Ge, which causes $CsSnI_3$ to have a larger unit cell volume (1686.9281 Å^3) compared to $CsGeI_3$ (1463.1486 Å^3).

These results are consistent with experimental and theoretical values [64, 75–80], although minor discrepancies exist due to the computational methods employed, which can introduce small variations depending on exchange-correlation functionals. $CsGeI_3$ has a bulk modulus of 17.5930 GPa, indicating that it is slightly stiffer than $CsSnI_3$, which has a bulk modulus of 15.2334 GPa. A lower bulk modulus in $CsSnI_3$ suggests a material that is more compressible, consistent with the larger atomic size of Sn, which leads to weaker bonds between atoms.

Additionally, the pressure derivative of the bulk modulus (B′) provides insights into how the material's compressibility changes under pressure. The value for $CsGeI_3$ is 4.9865, which is slightly higher than that for $CsSnI_3$ (3.5259). This suggests that $CsGeI_3$ will experience a more significant increase in resistance to compression as pressure increases compared to $CsSnI_3$. When compared to other works, the lattice constants and bulk moduli for both $CsGeI_3$ and $CsSnI_3$ show reasonable agreement, although slight

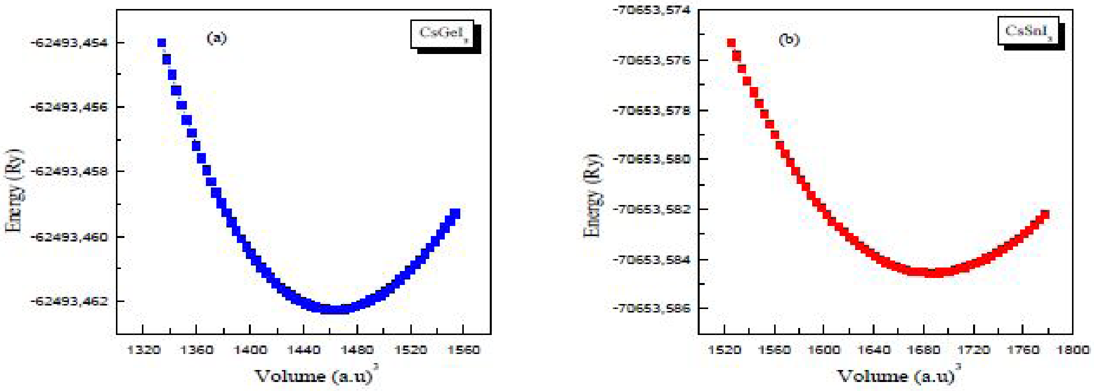

Fig. 7 The total energy as a function of volume for (a) $CsGeI_3$ and (b) $CsSnI_3$

Table 3 The lattice parameters, bulk modulus, pressure derivative (B′), and formation energy (E_f) for $CsGeI_3$ and $CsSnI_3$

Compound		V0 (a.u)^3	a0 (Å)	B0 (GPa)	B′	E0 (Ry)	Eg (eV)
$CsGeI_3$	This work	1463.14	6.00	17.59	4.98	−62493.46	0.71
	Other Exp	1451.36^a	5.991^a	16.60^a		−62493.39^a	0.62^e
	This work		6.05^b				1.60^f
$CsSnI_3$		1686.92	6.29	15.23	3.52	−70653.58	0.69
	Other Exp		6.245^c	16.56^c	4.27^c	−70653.52^c	0.44^c
			6.21^d				1.27^g

Notes: a: [68], b: [69], c: [70], d: [71], e: [72], f: [73], g: [74]

variations are observed due to different computational approaches. For instance, other studies report a lattice constant of 5.98 Å for $\mathrm{CsGeI_3}$, which is slightly lower than our computed value of 6.0075 Å. Similarly, the bulk modulus for $\mathrm{CsSnI_3}$ reported in other work (22.70 GPa) is higher than our calculated value of 15.2334 GPa, possibly due to different treatment of the exchange-correlation effects.

3.2.2 Elastic, mechanical and thermodynamic properties

The elastic constants are essential in evaluating a material's mechanical response and resilience under different stress conditions, offering valuable information about its potential for structural and mechanical applications. For cubic crystals, mechanical stability depends on three key elastic constants: C_{11}, C_{12}, and C_{44}. These constants, obtained from the second derivative of the total energy with respect to strain, are essential for assessing stability via the Born criteria [81]:

$$C_{11} - C_{12} > 0 \tag{4}$$

$$C_{11} > 0 \tag{5}$$

$$C_{44} > 0 \tag{6}$$

and

$$C_{11} + 2C_{12} > 0 \tag{7}$$

From these values, the bulk modulus B, shear modulus G [83], and Young's modulus E are calculated utilizing the Voigt-Reuss-Hill averaging approach [68]. In cubic systems, the bulk modulus is estimated as follows [48]:

$$Bv = 1/3\left(C_{11} + C_{12}\right) \tag{8}$$

Shear modulus, Young's modulus, and Poisson's ratio (v\nuv) are calculated using:

$$Y = \frac{9BG}{\left(3B + G'\right)}, \quad v = \frac{\left(3B - 2G\right)}{\left(2\left(3B + G\right)\right)} \tag{9}$$

The anisotropy factor A and Pugh's ratio B/G further characterize the elastic behavior. A, defined as:

$$A = \left(2C_{44}\right) / \left(C_{11} + C_{12}\right) \tag{10}$$

assesses elastic anisotropy, while Pugh's ratio B/G indicates ductility; values above 1.75 suggest ductile behavior [69], while values below 1.75 indicate brittleness [70].

Elastic constant

For $\mathrm{CsGeI_3}$, the elastic constants C_{11}, C_{12}, and C_{44} are 36.554 GPa, 4.415 GPa, and 8.387 GPa, respectively, as detailed in Table 4 [71, 78]. These values indicate relatively higher stiffness along the [1 0 0] direction, which is consistent with its cubic symmetry. In comparison, $\mathrm{CsSnI_3}$ has lower elastic constants with C_{11} = 28.860 GPa, C_{12} = 4.582 GPa, and C_{44} = 7.313 GPa, implying that $\mathrm{CsSnI_3}$ is more flexible and softer than $\mathrm{CsGeI_3}$. These values suggest that $\mathrm{CsGeI_3}$ exhibits better resistance to deformation under stress compared to $\mathrm{CsGeI_3}$. When comparing with previous works, the elastic constants for $\mathrm{CsGeI_3}$ are slightly lower than those reported in literature (C_{11} = 40.32GPa, C_{12} = 8.18 GPa), but remain in the same order of magnitude, reflecting minor discrepancies potentially arising from different computational approaches, which is in very agrrement with other work [72, 78].

Resistance to compression and shear response

The bulk modulus (B) quantifies how a material withstands isotropic compression, is 15.127 GPa for $\mathrm{CsGeI_3}$, while

Table 4 Elastic and mechanical properties of $\mathrm{CsGeI_3}$ and $\mathrm{CsSnI_3}$, showcasing parameters such as Young's modulus, shear modulus, and poisson's ratio

Parameters	$\mathrm{CsGeI_3}$	Other work [79]	$\mathrm{CsSnI_3}$	Other work [72]
C_{11}	36.55	40.15	28.86	33.59
C_{12}	4.41	6.84	4.58	16.79
C_{44}	8.38	8.51	7.31	8.65
Bulk modulus B	15.12	17.98	12.67	15.57
Shear modulus G (GPa)	10.91	11.17	8.96	8.78
Young modulus Y (GPa)	26.39	27.76	21.76	22.19
Pugh ratio B/G	1.38	1.61	1.41	1.77
Poisson ratio v	0.20	0.24	0.21	0.26
Anisotropy factor A	0.52	0.51	0.60	-
$C_{12} - C_{44}$	−3.97	−1.67	−2.73	8.11
Melting temperature T_m (K)	769.03 + 300 K	790.31 + 300 K	723.56 + 300 K	-

$CsSnI_3$ exhibits a lower bulk modulus of 12.674 GPa. This difference indicates that $CsGeI_3$ is less compressible than $CsSnI_3$, aligning with its higher stiffness. The shear modulus (G) of $CsGeI_3$ is also higher at 10.914 GPa compared to 8.968 GPa for $CsSnI_3$, suggesting stronger resistance to shape changes under shear stress for $CsGeI_3$. These moduli play a critical role in determining the mechanical robustness of materials under different stress conditions.

A comparative analysis of tensile stiffness

Young's modulus (Y) serves as an indicator of a material's tensile stiffness. In this context, $CsGeI_3$ exhibits a higher Young's modulus of 26.394 GPa, in contrast to $CsSnI_3$, which has a value of 21.769 GPa. This higher Young's modulus for $CsGeI_3$ confirms its superior mechanical strength, making it a more suitable candidate for applications where mechanical durability is essential. The literature shows slightly higher values for both materials, with $CsSnI_3$ having Y = 26.61 GPa, indicating that although our results show slight deviations, the trends remain consistent.

Pugh ratio (B/G) and ductility

Pugh's ratio (B/G) is a measure of a material's ductility. A value greater than 1.75 suggests ductile behavior, while a lower value indicates brittleness. $CsGeI_3$ has a Pugh ratio of 1.386, indicating brittle behavior, while $CsSnI_3$ has a value of 1.413, which also classifies it as brittle. However, when compared with other works, $CsSnI_3$ is closer to the ductile-brittle transition point with a reported Pugh ratio of 2.221, showing a more ductile character in previous studies. This discrepancy suggests that $CsSnI_3$ might exhibit varying ductile tendencies under different conditions.

Poisson's Ratio (ν), Anisotropy Factor (A), $C_{12} - C_{44}$ Difference and Melting Temperature (T_m)

The Poisson's ratio (ν) reflects the material's response in the transverse direction when subjected to longitudinal strain. $CsGeI_3$ has a Poisson's ratio of 0.209, while $CsSnI_3$ has a slightly higher value of 0.213, indicating that both materials exhibit similar deformation behaviors under applied stress. The values are consistent with the brittle nature of these compounds. Additionally, the anisotropy factor (A) for $CsGeI_3$ is 0.521, slightly lower than the 0.602 for $CsSnI_3$, which indicates that $CsSnI_3$ has a more pronounced directional dependence of its elastic properties, making it slightly more anisotropic compared to $CsGeI_3$. Typically, for materials governed by central forces, ν falls between 0.25 and 0.5 [72]. The anisotropy factor A measures the directional dependence of the elastic properties. For isotropic materials, A equals 1, while deviations from this value indicate anisotropy.

The melting temperature (T_m) is a critical parameter in evaluating the thermal stability of materials.

Lastly, these values were calculated using empirical relationships between the elastic properties and melting behavior of the compounds [73]:

$$T_m\left(K\right) = \left[553\left(K\right) + \left(5.911\right)C_{12}\right] GPa \pm 300K \tag{11}$$

High melting temperatures indicate good thermal resistance, making these materials suitable for high-temperature applications. The melting temperature (T_m) calculated for $CsGeI_3$ is 769.0347 K, significantly higher than the melting temperature of $CsSnI_3$ at 723.5626 K. This reinforces the observation that $CsGeI_3$ is structurally more robust than $CsSnI_3$, making it more thermally stable, which is beneficial for high-temperature applications. In summary, $CsGeI_3$ shows higher stiffness, greater mechanical strength, and enhanced thermal stability compared to $CsSnI_3$. Both materials exhibit brittle behavior, though $CsSnI_3$ appears to be closer to the ductile-brittle transition in some cases. These properties highlight $CsGeI_3$ as a stronger candidate for applications requiring higher mechanical and thermal robustness.

$$\begin{gathered} v_1 = \left(\left(3B + 4G\right) / 3\rho\right)^{1/2}, \; v_t = \left(G / \rho\right)^{1/2}, \\ v_m = \left[1/3\left(2/v_t^3 + 1/v_1^3\right)\right]^{-1/3} \end{gathered} \tag{12}$$

Furthermore, the Debye temperature (θ_D), a measure related to the material's thermal properties, is obtained based on the mean sound velocity. This temperature indicates the material's phonon behavior and is calculated through the following expression, which incorporates both the elastic properties and atomic mass [83]:

$$\theta_D = h / k_B \left[3n / 4\pi\left(\left(N_A \rho\right) / M\right)\right]^{1/3 v_m} \tag{13}$$

The transverse and longitudinal sound velocities are critical parameters in determining the elastic behavior and thermal conductivity of materials, as summarized in Table 5. For $CsGeI_3$, the transverse sound velocity (v_1)

Table 5 The calculated sound velocities and Debye temperatures of $CsGeI_3$ and $CsSnI_3$

Parameters	$CsGeI_3$	$CsSnI_3$
Transverse sound velocity v_t (m/s)	1559.07	1460.19
Longitudinal sound velocity v_t (m/s)	2571.01	2419.95
Average sound velocity v_m (m/s)	1722.9	1614.43
Debye temperature (θ_D) (K)	146.00	133.86

is 1559.07 m s^{-1}, while the longitudinal sound velocity (v_l) is 2571.01 m s^{-1}. In comparison, $CsSnI_3$ has slightly lower values, with v_m = 1460.19 m.s^{-1} and v_m = 2419.95 m.s^{-1}. The average sound velocity (v_m), calculated from the transverse and longitudinal velocities, gives an overall indication of how sound propagates through the material. $CsGeI_3$ exhibits a higher average sound velocity (v_m = 1722.9 m s^{-1}) compared to $CsSnI_3$ (v_m = 1614.43 m s^{-1}), confirming its stiffer lattice and stronger interatomic bonds. These sound velocity values suggest that $CsGeI_3$ would transmit sound waves more efficiently, which is associated with stronger atomic interactions and a more tightly bonded crystal structure.

The Debye temperature (θ_D) is a crucial parameter related to the vibrational properties of the crystal lattice, heat capacity, and thermal conductivity. It is directly proportional to the average sound velocity, reflecting the material's stiffness and bond strength. For $CsGeI_3$, the Debye temperature is 146.004 K, while for $CsSnI_3$, it is slightly lower at 133.864 K. A higher Debye temperature indicates that $CsGeI_3$ has stiffer bonds and a higher thermal stability compared to $CsSnI_3$. The Debye temperature also provides information on the temperature range over which the material exhibits quantum mechanical behavior, where specific heat decreases with temperature. Since $CsGeI_3$ has a higher θ_D, it will remain in this quantum mechanical regime at higher temperatures compared to $CsSnI_3$, making it more suitable for applications requiring stability under high thermal loads.

3.3 Electronic properties

The bandgap energy plays a crucial role in determining the material's optical and electronic properties, specifically for optoelectronic applications. The relatively narrow bandgap of $CsGeI_3$ suggests that it can absorb a wide range of the visible spectrum, making it suitable for photovoltaic applications. Additionally, a reduced bandgap typically correlates with an increased density of electronic states around the Fermi level, facilitating greater carrier mobility and potentially enhancing electrical conductivity. This characteristic is particularly advantageous for technologies such as solar cells, where effective transport of charge carriers is crucial. The analysis of the band structure for $CsGeI_3$, conducted using both GGA and GGA-mBJ methods, reveals the presence of a direct bandgap, as illustrated in Fig. 8. The GGA approximation yields a bandgap of 0.65 eV, while the more accurate GGA-mBJ approximation gives a slightly higher value of 0.71 eV. This increase in the bandgap with GGA-mBJ is consistent with its improved handling of electronic correlations and exchange interactions, which often results in a better match to experimental values and theoretical work [84–86]. It is widely recognized that the Generalized Gradient Approximation (GGA) tends to yield lower estimates of the electronic band gap, especially in the case of semiconductors and insulators [87, 88]. The electronic band structures of $CsSnI_3$ using the same computational methods, with the Fermi level shown as a dotted line for reference is plotted in Fig. 9.

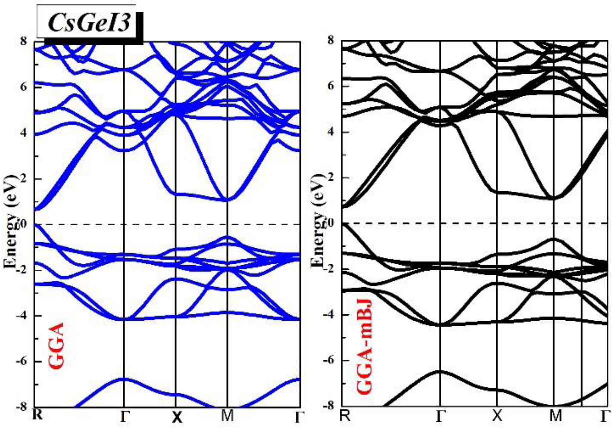

Fig. 8 The electronic band structures of $CsGeI_3$ calculated with GGA and GGA-mBJ approaches at equilibrium, with the dotted line indicating the Fermi level

For $CsSnI_3$, the band structure also exhibits a direct band gap, with values of 0.50 eV using GGA and 0.69 eV with GGA-mBJ, as shown in Fig. 8.

The increase in the bandgap when using GGA-mBJ reflects the method's ability to account for the electronic structure more accurately. This direct bandgap implies that photon absorption in $CsSnI_3$ can occur without phonon

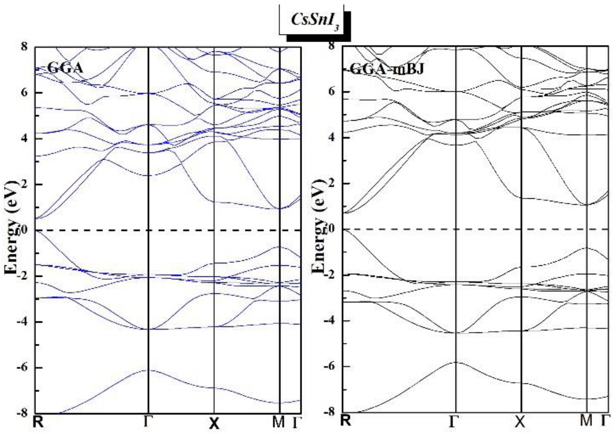

Fig. 9 The electronic band structures of $CsSnI_3$ using the same computational methods, with the Fermi level shown as a dotted line for reference

assistance, which enhances its efficiency in optoelectronic devices compared to materials with an indirect bandgap. In Ge-based compounds, the electronic band gaps are typically larger compared to those found in Sn-based counterparts. This difference arises because the conduction band edge in Ge-containing materials tends to shift towards higher energies [89]. This upward shift results from the smaller atomic radius of Ge, which leads to greater orbital overlap and hence a wider band gap. This trend is characteristic of this class of materials, where the substitution of Ge for Sn generally increases the band gap, influencing their electronic properties and potential applications in optoelectronics. Our calculated band gaps (0.71 eV for $CsGeI_3$ and 0.68 eV for $CsSnI_3$) align closely with other theoretical works that also use standard DFT methods, though as mentioned, these results typically underestimate the actual values. For example, other computational studies using similar GGA approaches report band gaps for $CsGeI_3$ around 0.62 eV and for $CsSnI_3$ around 0.44 eV, both of which are even lower than our calculated values. This underestimation highlights the importance of using more accurate methods for band gap prediction when designing materials for practical applications. The low GGA and GGA-mBJ bandgap values for $CsGeI_3$ (0.71 eV) and $CsSnI_3$ (0.69 eV) arise from the well-known underestimation of bandgaps by standard DFT methods. While experimental values are typically >1.1 eV, our use of the mBJ potential improves accuracy but still lacks many-body corrections like GW. Nonetheless, our results align well with other theoretical works and provide reliable insights into the electronic structure and optical transitions of these materials.

Both $CsGeI_3$ and $CsSnI_3$ exhibit small bandgaps, making them suitable candidates for light absorption and utilization in energy conversion applications, particularly in the near-infrared region. The difference in their bandgap values and response to different computational methods reflects the subtle variations in their electronic structures, which can influence device performance. $CsGeI_3$ with its slightly larger bandgap might offer better thermal stability and lower leakage currents, while $CsSnI_3$ could provide better infrared absorption.

Analyzing the density of states (DOS) offers critical information regarding the electronic characteristics of $CsGeI_3$ and $CsSnI_3$. Here's a detailed discussion of each material's DOS, investigating the roles of different atomic orbitals and their relevance to the band structure is essential. The density of states (DOS) analysis for $CsGeI_3$ indicates its semiconducting behavior, with band gap values of 0.65 eV and 0.71 eV obtained from the GGA and GGA-mBJ methods, respectively, as shown in Fig. 10. Within the valence band region, the Iodine (I) *p* orbitals primarily govern the DOS, while the Germanium (Ge) *p* orbitals contribute minimally, underscoring the dominant influence of Iodine in shaping the characteristics of the valence band. The conduction band, on the other hand, is largely influenced by (Ge) *p* states, with a slight contribution from Cesium (Cs) orbitals. This distribution suggests that upon excitation, electrons primarily transition from I *p* orbitals to Ge *p* orbitals, characterizing the material's charge-transfer nature. The presence of a narrow band gap suggests potential applications in infrared optoelectronic devices, where lower-energy photons can be absorbed. The DOS profile of $CsSnI_3$ also indicates semiconducting behavior, with band gaps of 0.50 eV (GGA) and 0.69 eV (GGA-mBJ), as shown in Fig. 11. Similar to $CsGeI_3$, the valence band is dominated by I *p* orbitals, while the conduction band shows significant contributions from Tin (Sn) *p* states. Additionally, Sn *s* orbitals contribute slightly below the Fermi level, indicating a strong covalent interaction with I *p* states. This interaction enhances the valence band's stability and supports effective electronic transitions across the band gap. The narrow band gap of $CsSnI_3$, especially under mBJ correction, suggests its utility in near-infrared optoelectronic applications, where the material can effectively absorb photons of lower energy. The notable presence of Sn in the conduction band further implies potential for high electronic mobility, which is advantageous for applications requiring efficient charge transport.

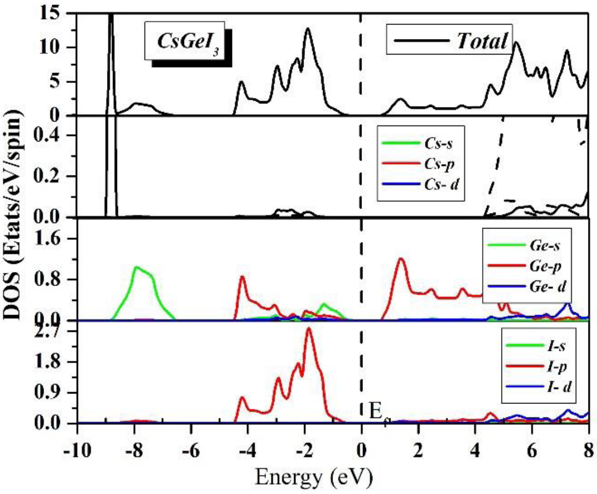

Fig. 10 The total and partial density of states (DOS) for $CsGeI_3$, showing the contributions of different atoms and orbitals to the electronic states near the Fermi level

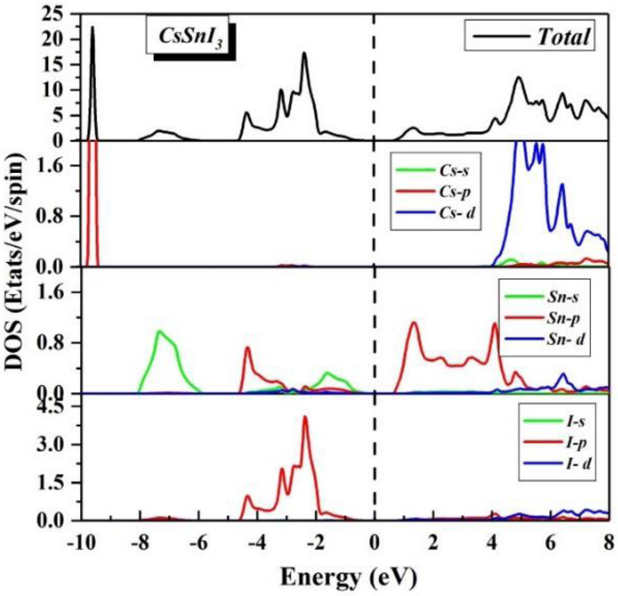

Fig. 11 The total and partial density of states (DOS) for CsSnI$_3$, showing the contributions of different atoms and orbitals to the electronic states near the Fermi level

3.4 Optical behavior

The optical behavior of CsGeI$_3$ and CsSnI$_3$ was analyzed using the GGA-mBJ method within the WIEN2k framework, aimed at assessing their suitability for optoelectronic applications. The assessment of the complex dielectric function, expressed as $\varepsilon(\omega) - \varepsilon_1(\omega) + i\varepsilon_2(\omega)$ [71, 90–96], sheds light on the interaction of these materials with electromagnetic radiation at varying photon energies, ω. In this context, $\varepsilon_1(\omega)$ represents the material's dispersion properties, while $\varepsilon_2(\omega)$ reflects its ability to absorb light. Important optical parameters, including the refractive index $n(\omega)$, extinction coefficient $k(\omega)$, reflectivity $R(\omega)$, and absorption coefficient $\alpha(\omega)$, were derived from the dielectric function, providing a detailed understanding of their optoelectronic characteristics. The refractive index and extinction coefficient are crucial for analyzing the propagation of light and the mechanisms of loss within the material [95–100]:

$$n(\omega)=1/\sqrt{2}\left[\left(\varepsilon_1^2(\omega)+\varepsilon_2^2(\omega)\right)^{\frac{1}{2}}+\varepsilon_1(\omega)\right]^{\frac{1}{2}} \tag{14}$$

$$k(\omega)=1/\sqrt{2}\left[\left(\varepsilon_1^2(\omega)+\varepsilon_2^2(\omega)\right)^{\frac{1}{2}}+\varepsilon_1(\omega)\right]^{\frac{1}{2}} \tag{15}$$

$$R(\omega)=\left|\left(\sqrt{\left(\varepsilon(\omega)\right)}-1\right)/\left(\sqrt{\left(\varepsilon(\omega)\right)}+1\right)\right|^2 \tag{16}$$

3.4.1 Dielectric function

The real component of the dielectric function, $\varepsilon_1(\omega)$, illustrated in Fig. 12(a) demonstrates the dispersive characteristics of CsGeI$_3$ and CsSnI$_3$, revealing how these materials respond to external electric fields. In both cases, $\varepsilon_1(\omega)$ exhibits a notable peak in the lower energy spectrum. For CsGeI$_3$, this peak occur around 2 eV, with a value that slightly exceeds that of CsSnI$_3$, indicating enhanced dispersion and polarizability. This suggests that CsGeI$_3$ has a marginally higher capacity to store electrical energy in this region. As the energy increases, $\varepsilon_1(\omega)$ diminishes, crossing zero at approximately 10 eV for both materials, marking the plasma edge. Beyond this threshold, CsGeI$_3$ and CsSnI$_3$ behave similarly to transparent dielectrics, as they cease to support free-electron oscillations at elevated photon energies.

The imaginary part of the dielectric function, $\varepsilon_2(\omega)$ shown in Fig. 12(b), pertains to the absorption properties of the materials, indicating electronic transitions from the valence band to the conduction band. Both CsGeI$_3$ and CsSnI$_3$ display significant peaks in $\varepsilon_2(\omega)$ within the energy interval of 2 to 6 eV. CsGeI$_3$ exhibits a slightly higher peak than CsSnI$_3$, indicating that CsGeI$_3$ has a higher absorption capacity at these energies, which could be advantageous for applications requiring efficient light absorption. Both materials exhibit multiple absorption peaks within this range, corresponding to transitions involving different electronic states. These strong absorptive features suggest that CsGeI$_3$ and CsSnI$_3$ are well-suited for optoelectronic applications, particularly in the visible spectrum, with CsGeI$_3$ showing a marginally stronger absorption profile.

3.4.2 Absorption coefficient and optical conductivity (σ)

The optical conductivity spectra of CsGeI$_3$ and CsSnI$_3$, as illustrated in Fig. 12(c), provide insights into their electronic response under optical excitation. Both materials exhibit notable peaks within the energy range of 2 to 12 eV, indicating strong optical transitions. For CsGeI$_3$, the maximum optical conductivity reaches around 4500 $(\Omega\ \mathrm{cm})^{-1}$ at approximately 9 eV, whereas CsSnI$_3$ shows a slightly high peak conductivity of about 5200 $(\Omega\ \mathrm{cm})^{-1}$ in the same energy range. These peaks correspond to interband transitions and reflect the materials' ability to conduct electrical currents under light exposure. The higher optical conductivity of CsGeI$_3$ suggests it may offer better performance in optoelectronic devices, as it implies a greater capacity for photon-induced charge carrier movement. Both materials show multiple peaks, with a slight red shift for CsSnI$_3$, indicative of the differing band structures and transition energies.

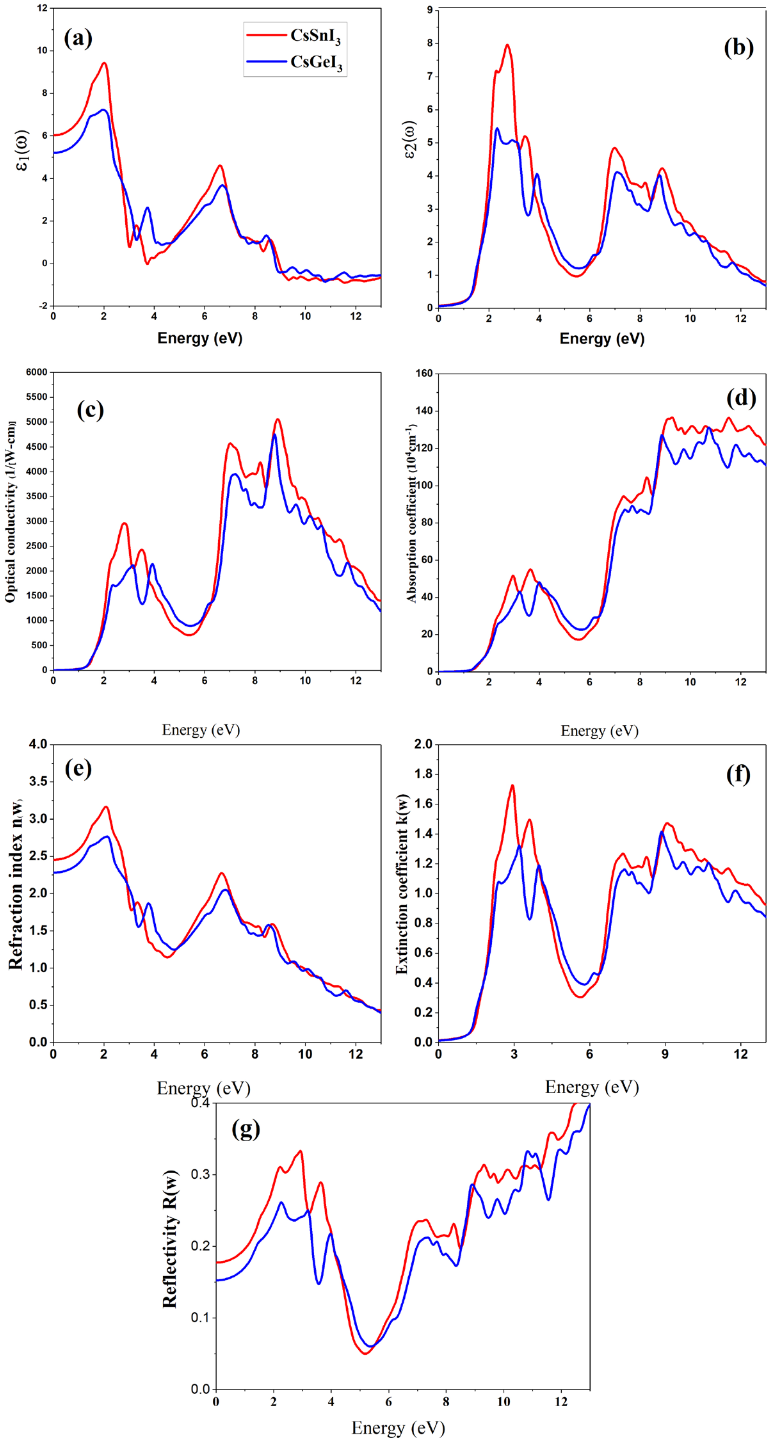

Fig. 12 Provides (a) the real part of the dielectric function $\varepsilon_1(\omega)$, (b) the imaginary part $\varepsilon_2(\omega)$, (c) the absorption coefficient $\alpha(\omega)$, (d) the refractive index $n(\omega)$, (e) the extinction coefficient $k(\omega)$, and (f) the reflectivity $R(\omega)$ as functions of photon energy (eV) for $CsGeI_3$ and $CsSnI_3$

The absorption coefficient, α, indicates the extent to which $CsGeI_3$ and $CsSnI_3$ absorb light at varying photon energies, a factor that is vital for their use in photovoltaic and photodetector applications, as shown in Fig. 12(d). For both compounds, α shows a marked increase past 2 eV, peaking at approximately 120 cm^{-1} for $CsGeI_3$ and 140 cm^{-1} for $CsSnI_3$ in the 8 to 10 eV energy range. This elevated absorption level signifies a strong interaction with both visible and ultraviolet light, positioning these materials as promising candidates for devices that require effective light absorption. The higher absorption coefficient of $CsGeI_3$, particularly in the ultraviolet range, suggests it may be more effective in applications requiring UV light capture. This behavior is consistent with the observed electronic band gaps, where has slightly higher photon absorption capacity, enhancing its suitability for optoelectronic applications. Although excitonic effects and carrier diffusion lengths were not directly computed in this study, the strong absorption onset near the band edges and the absence of distinct excitonic peaks suggest that exciton binding energies are relatively low, favoring spontaneous exciton dissociation into free charge carriers. Furthermore, the high optical conductivity values observed – especially for $CsGeI_3$ – imply efficient charge carrier transport and reduced recombination losses. These features point toward favorable conditions for long diffusion lengths, making these materials strong candidates for use as absorber layers in perovskite-based photovoltaic and optoelectronic systems.

3.4.3 Refractive index and extinction coefficient

The refractive index spectra of $CsGeI_3$ and $CsSnI_3$ exhibit similar trends across the photon energy range, with both materials showing high refractive indices at lower energies, which gradually decrease as the photon energy increases, as depicted in Fig. 12(e). $CsGeI_3$ reaches a peak refractive index of approximately 2.7 around 2 eV, while $CsSnI_3$ peaks slightly lower at around 3.25 eV. These values indicate that $CsGeI_3$ and $CsSnI_3$ have strong polarizability and a high capacity for light bending, which are advantageous for optoelectronic applications such as waveguides and lenses. As the energy exceeds 6 eV, the refractive indices for both materials start to converge towards 2.0, reflecting a reduction in optical density and indicating a transition to more transparent behavior at higher energies.

The extinction coefficient, which signifies the amount of light attenuation within the material, shows significant peaks for both $CsGeI_3$ and $CsSnI_3$, particularly between 2 and 8 eV, as shown in Fig. 12(f). $CsGeI_3$ has a peak extinction coefficient of about 1.3 near 3 eV, while $CsSnI_3$ reaches a maximum of around 1.7 at a slightly lower energy level. This behavior suggests that $CsGeI_3$ has a higher capacity for absorbing light in the visible region, making it potentially more effective in applications requiring high light absorption, such as photovoltaic cells. Beyond 6 eV, both materials display a gradual decline in the extinction coefficient, indicating diminished absorption in the ultraviolet range and signifying a reduction in photon energy dissipation within these materials.

3.4.4 Reflectivity

The reflectivity spectra of $CsGeI_3$ and $CsSnI_3$ exhibit characteristic peaks and troughs across the energy range, which offer insights into their optical behavior, as illustrated in Fig. 12(g). For $CsGeI_3$, the reflectivity starts at around 0.15 in the low-energy region and reaches its minimum value of approximately 0.06 near 5 eV. The material then demonstrates a noticeable increase in reflectivity, peaking at about 0.4 at energies beyond 12 eV. This trend suggests that $CsGeI_3$ has lower reflectivity in the visible range, which indicates higher light absorption and less surface reflection, making it suitable for applications in solar cells where minimizing reflection is beneficial for enhanced photon absorption.

In contrast, $CsSnI_3$ starts with a slightly higher initial reflectivity of around 0.18, with a gradual decrease to its minimum value of about 0.05 near 5 eV. $CsSnI_3$ then exhibits an increase similar to $CsGeI_3$, though it peaks at a slightly lower reflectivity of around 0.38 at energies exceeding 12 eV. The reflectivity of $CsSnI_3$ remains generally lower than $CsGeI_3$ in the 4-6 eV range, indicating that it may be slightly more effective in absorbing light within the visible region. This behavior aligns with its potential use in optoelectronic devices where reduced reflection can improve device efficiency. The higher reflectivity at energies above 10 eV for both materials indicates increased reflection in the ultraviolet region, which could be advantageous for UV-blocking applications.

4 Conclusion

In conclusion, this work provided a comprehensive evaluation of the lead-free perovskites $CsGeI_3$ and $CsSnI_3$ by combining SCAPS-1D device simulations with detailed DFT calculations. The SCAPS-1D analysis of the Au/CuI/$CsGeI_3$/$CsSnI_3$/ZnSe/FTO solar cell revealed that optimal photovoltaic performance was achieved using a $CsGeI_3$ absorber thickness of 1000 nm and a $CsSnI_3$ layer thickness of 700 nm, with both perovskites doped at 10^{19} cm^{-3} and having a defect density of 10^{14} cm^{-3}. Under these optimized conditions, the device delivered an open-circuit voltage (Voc) of 1.17534 V, a short-circuit current density (Jsc) of 30.54 mA cm^{-2}, a fill factor (FF) of 88.08%, and an overall power conversion efficiency (PCE) of 31.61%. These values highlight the strong photovoltaic potential of combining $CsGeI_3$ and $CsSnI_3$ within a single device architecture. The DFT results further corroborated these findings by confirming the structural, mechanical, and electronic suitability of both materials. $CsGeI_3$ and $CsSnI_3$ exhibited stable cubic structures with optimized lattice parameters consistent with reported values, while their elastic constants, bulk modulus, shear modulus, and Young's modulus verified their mechanical stability and ductile nature. Thermodynamic parameters including sound velocities and Debye temperatures also supported their structural robustness. Furthermore, the electronic structure calculations revealed narrow band gaps of 0.71 eV for $CsGeI_3$ and 0.69 eV for $CsSnI_3$ (mBJ), making them promising absorbers for visible and near-infrared light. Overall, the excellent photovoltaic metrics obtained through SCAPS simulations, together with the favorable structural and electronic properties from DFT, confirm that $CsGeI_3$ and $CsSnI_3$ are strong lead-free candidates for next-generation, high-efficiency solar cells and optoelectronic devices. Future investigations may explore interface engineering, dopant tuning, and long-term stability to support experimental realization and further improve device performance.

Acknowledgments

The work is included in the PRFU 2022 project under contract number B00L02UN310220220001.

References

[1] Ye, T., Wang, K., Hou, Y., Yang, D., Smith, N., Magill, B., Yoon, J., Mudiyanselage, R. R. H. H., Khodaparast, G. A., Priya, S. "Ambient-Air-Stable Lead-Free $CsSnI_3$ Solar Cells with Greater than 7.5% Efficiency", Journal of the American Chemical Society, 143(11), pp. 4319–4328, 2021. https://doi.org/10.1021/jacs.0c13069

[2] Stranks, S. D., Snaith, H. J. "Metal-halide perovskites for photovoltaic and light-emitting devices", Nature Nanotechnology, 10(5), pp. 391–402, 2015. https://doi.org/10.1038/nnano.2015.90

[3] Zhou, Y., Zhu, K. "Perovskite Solar Cells Shine in the 'Valley of the Sun'", ACS Energy Letters, 1(1), pp. 64–67, 2016. https://doi.org/10.1021/acsenergylett.6b00069

[4] Islam, M. R., Mazumder, A. A. M., Mojumder, M. R. H., Shifat, A. S. M. Z., Hossain, M. K. "Strain-induced tunable optoelectronic properties of inorganic halide perovskites $APbCl_3$ (A = K, Rb, and Cs)", Japanese Journal of Applied Physics, 62(1), 011002, 2023. https://doi.org/10.35848/1347-4065/acb09e

[5] Thakur, A., Singh, D., Kaur, S. "Numerical simulations of 26.11% efficient planar $CH_3NH_3PbI_3$ perovskite *n*–i–p solar cell", Materials Today: Proceedings, 71, pp. 195–201, 2022. https://doi.org/10.1016/j.matpr.2022.08.423

[6] Zhang, W., Eperon, G. E., Snaith, H. J. "Metal halide perovskites for energy applications", Nature Energy, 1(6), 16048, 2016. https://doi.org/10.1038/nenergy.2016.48

[7] Swarnkar, A., Marshall, A. R., Sanehira, E. M., Chernomordik, B. D., Moore, D. T., Christians, J. A., Chakrabarti, T., Luther, J. M. "Quantum dot–induced phase stabilization of α-$CsPbI_3$ perovskite for high-efficiency photovoltaics", Science, 354(6308), pp. 92–95, 2016. https://doi.org/10.1126/science.aag2700

[8] Yin, W.-J., Shi, T., Yan, Y. "Unique properties of halide perovskites as possible origins of the superior solar cell performance", Advanced Materials, 26(27), pp. 4653–4658, 2014. https://doi.org/10.1002/adma.201306281

[9] Marshall, K. P., Walker, M., Walton, R. I., Hatton, R. A. "Enhanced stability and efficiency in hole-transport-layer-free $CsSnI_3$ perovskite photovoltaics", Nature Energy, 1(12), 16178, 2016. https://doi.org/10.1038/nenergy.2016.178

[10] Sutton, R. J., Eperon, G. E., Miranda, L., Parrott, E. S., Kamino, B. A., Patel, J. B., Hörantner, M. T., Johnston, M. B., Haghighirad, A. A., Moore, D. T., Snaith, H. J. "Bandgap-Tunable Cesium Lead Halide Perovskites with High Thermal Stability for Efficient Solar Cells", Advanced Energy Materials, 6(8), 1502458, 2016. https://doi.org/10.1002/aenm.201502458

[11] Hoffman, J. B., Schleper, A. L., Kamat, P. V. "Transformation of Sintered $CsPbBr_3$ Nanocrystals to Cubic $CsPbI_3$ and Gradient $CsPbBr_xI_{3-x}$ through Halide Exchange", Journal of the American Chemical Society, 138(27), pp. 8603–8611, 2016. https://doi.org/10.1021/jacs.6b04661

[12] Huang, L., Lambrecht, W. R. L. "Electronic band structure trends of perovskite halides: Beyond Pb and Sn to Ge and Si", Physical Review B, 93(19), 195211, 2016. https://doi.org/10.1103/PhysRevB.93.195211

[13] Asiri, A. M., Shahzad, M. K., Hussain, S., Zhu, K., Khan, S. B., Alamry, K. A., Alfifi, S. Y., Marwani, H. M. "Analysis of $XGaO_3$ (X = Ba and Cs) cubic perovskite materials for photocatalytic water splitting applications: A DFT study", Heliyon, 9(3), e14112, 2023. https://doi.org/10.1016/j.heliyon.2023.e14112

[14] Khan, A. A., Noman, M., Jan, S. T. "Investigating the compatibility of kesterite and zinc charge transport layers with inorganic germanium perovskite solar cells", Optical and Quantum Electronics, 57(1), 114, 2025. https://doi.org/10.1007/s11082-024-08022-x

[15] Ahmad, A., Jan, S. T., Khan, H. A., Sheraz, M., Tareen, W. U. K., Chuah, T. C., Lee, I. E., Ali, H. "Compatibility analysis of novel inorganic cesium perovskites with emerging charge transport layers through design optimization", Energy Nexus, 17, 100400, 2025. https://doi.org/10.1016/j.nexus.2025.100400

[16] Gautam, S., Gupta, D. C. "Exploring the structural, mechanical, electronic, thermodynamic and thermoelectric properties of caesium-based ABX_3 perovskite $CsOsX_3$ (X = Cl, Br)", RSC Advances, 14(34), pp. 24977–24984, 2024. https://doi.org/10.1039/d4ra04628e

[17] Murtaza, H., Ain, Q., Munir, J., Ghaithan, H. M., Ali, M., Ahmed, A. A. A., Qaid, S. M. H. "Tuning the thermoelectric and optoelectronic attributes of lead-free novel fluoroperovskites $Cs_2BB'F_6$ (B = Rb, In, Na; B' = Ir, As, Rh): A first-principles investigation", Journal of Physics and Chemistry of Solids, 190, 111934, 2024. https://doi.org/10.1016/j.jpcs.2024.111934

[18] Mbilo, M., Musembi, R., Kachira, P. J., Nyangau, W., Mugwanga, F., Edwin, R. "Insights into the optoelectronic and thermoelectric properties of lead-free Rb_2NaIrF_6 double perovskite compound: A first-principles study", Results in Physics, 75, 108349, 2025. https://doi.org/10.1016/j.rinp.2025.108349

[19] Ali, M. L., Khan, M., Al Asad, M. A., Rahaman, M. Z. "Highly efficient and stable lead-free cesium copper halide perovskites for optoelectronic applications: A DFT-based study", Heliyon, 9(8), e18816, 2023. https://doi.org/10.1016/j.heliyon.2023.e18816

[20] Shakeel, S., Song, P., Shah, S. H., Zada, Z., Huang, T., Laref, A., Hakimi, N., Faizan, M. "DFT analysis of elastic and optoelectronic properties of Cs_2NaXCl_6 (X = In, La, Sc, Y) double perovskite compounds", Materials Chemistry and Physics, 324, 129683, 2024. https://doi.org/10.1016/j.matchemphys.2024.129683

[21] Arif, M., Reshak, A. H., Zaman, S. U., Husain, M., Rahman, N., Ahmad, S. A., Saqib, M., Khan, S., Ramli, M. M., Khan, A. "Density functional theory based study of the physical properties of cesium based cubic halide perovskites $CsHgX_3$ (X = F and Cl)", International Journal of Energy Research, 46(3), pp. 2467–2476, 2022. https://doi.org/10.1002/er.7321

[22] Xiao, Z., Du, K.-Z., Meng, W., Wang, J., Mitzi, D. B., Yan, Y. "Intrinsic Instability of $Cs_2In(I)M(III)X_6$ (M = Bi, Sb; X = Halogen) Double Perovskites: A Combined Density Functional Theory and Experimental Study", Journal of the American Chemical Society, 139(17), pp. 6054–6057, 2017. https://doi.org/10.1021/jacs.7b02227

[23] Bhamu, K. C., Soni, A., Sahariya, J. "Revealing optoelectronic and transport properties of potential perovskites Cs_2PdX_6 (X = Cl, Br): A probe from density functional theory", Solar Energy, 162, pp. 336–343, 2018. https://doi.org/10.1016/j.solener.2018.01.059

[24] Ravindra, A. L. N. M. "Isosymmetric compression of cubic halide perovskites ABX_3 (A = K, Rb, Cs; B = Ge, Sn, Pb; X = Cl, Br, I) – influence of cation–anion exchange: a first principle study", SN Applied Sciences, 3(2), pp. 1–12, 2021. https://doi.org/10.1007/s42452-020-04059-1

[25] Jong, U.-G., Kim, Y.-S., Ri, C.-H., Kye, Y.-H., Yu, C.-J. "High Thermoelectric Performance in the Cubic Inorganic Cesium Iodide Perovskites $CsBI_3$ (B = Pb, Sn, Ge) from First-Principles", Journal of Physical Chemistry C, 125(11), pp. 6013–6019, 2021. https://doi.org/10.1021/acs.jpcc.0c09929

[26] Roknuzzaman, M., Ostrikov, K. K., Wang, H., Du, A., Tesfamichael, T. "Towards lead-free perovskite photovoltaics and optoelectronics by ab-initio simulations", Scientific Reports, 7(1), 14025, 2017. https://doi.org/10.1038/s41598-017-13172-y

[27] Khalil, R. M. A., Hayat, S., Hussain, M. I., Rana, A. M., Hussain, F. "DFT based first principles study of novel combinations of perovskite-type hydrides $XGaH_3$ (X = Rb, Cs, Fr) for hydrogen storage applications", AIP Advances, 11, 2021. https://doi.org/10.1063/5.0037790

[28] Noor, N. A., Iqbal, M. W., Zelai, T., Mahmood, A., Shaikh, H. M., Ramay, S. M., Al-Masry, W. "Analysis of direct band gap A_2ScInI_6 (A = Rb, Cs) double perovskite halides using DFT approach for renewable energy devices", Journal of Materials Research and Technology, 13, pp. 2491–2500, 2021. https://doi.org/10.1016/j.jmrt.2021.05.080

[29] Cao, D. H., Stoumpos, C. C., Yokoyama, T., Logsdon, J. L., Song, T.-B., Farha, O. K., Wasielewski, M. R., Hupp, J. T., Kanatzidis, M. G. "Thin Films and Solar Cells Based on Semiconducting Two-Dimensional Ruddlesden–Popper $(CH_3(CH_2)_3NH_3)_2(CH_3NH_3)_{n-1}Sn_nI_{3n+1}$ Perovskites", ACS Energy Letters, 2(5), pp. 982–990, 2017. https://doi.org/10.1021/acsenergylett.7b00202

[30] Hossain, M. K., Toki, G. F. I., Samajdar, D. P., Mushtaq, M., Rubel, M. H. K., Pandey, R., Madan, J., Mohammed, M. K. A., Islam, M. R., Rahman, M. F., Bencherif, H. "Deep Insights into the Coupled Optoelectronic and Photovoltaic Analysis of Lead-Free $CsSnI_3$ Perovskite-Based Solar Cell Using DFT Calculations and SCAPS-1D Simulations", ACS Omega, 8(25), pp. 22466–22485, 2023. https://doi.org/10.1021/acsomega.3c00306

[31] Dang, Y., Zhou, Y., Liu, X., Ju, D., Xia, S., Xia, H., Tao, X. "Formation of Hybrid Perovskite Tin Iodide Single Crystals by Top-Seeded Solution Growth", Angewandte Chemie International Edition, 55(10), pp. 3447–3450, 2016. https://doi.org/10.1002/anie.201511792

[32] Taghavi, M., Lee, C.-J. "Development of a novel hydrogen liquefaction structure based on liquefied natural gas regasification operations and solid oxide fuel cell: Exergy and economic analyses", Fuel, 384, 133826, 2025. https://doi.org/10.1016/j.fuel.2024.133826

[33] Taghavi, M., Yoon, H.-J., Choi, J.-U., Lee, C.-J. "Innovative Structure of a Liquefied Natural Gas (LNG) Process by Mixed Fluid Cascade Using Solar Renewable Energy, Photovoltaic Panels (PV), and Absorption Refrigeration System", Computer Aided Chemical Engineering, 53, pp. 2071–2076, 2024. https://doi.org/10.1016/B978-0-443-28824-1.50346-X

[34] Taghavi, M., Lee, C.-J. "Development of novel hydrogen liquefaction structures based on waste heat recovery in diffusion-absorption refrigeration and power generation units", Energy Conversion and Management, 302, 118056, 2024. https://doi.org/10.1016/j.enconman.2023.118056

[35] Taghavi, M., Salarian, H., Ghorbani, B. "Thermodynamic and exergy evaluation of a novel integrated hydrogen liquefaction structure using liquid air cold energy recovery, solid oxide fuel cell and photovoltaic panels", Journal of Cleaner Production, 320, 128821, 2021. https://doi.org/10.1016/j.jclepro.2021.128821

[36] Taghavi, M., Salarian, H., Ghorbani, B. "Economic Evaluation of a Hybrid Hydrogen Liquefaction System Utilizing Liquid Air Cold Recovery and Renewable Energies", Renewable Energy Research and Applications, 4(1), pp. 125–143, 2023. https://doi.org/10.22044/rera.2022.11899.1122

[37] Soonmin, H., Taghavi, M. "Solar Energy Development: Study Cases in Iran and Malaysia", International Journal of Engineering Trends and Technology, 70(8), pp. 408–422, 2022. https://doi.org/10.14445/22315381/IJETT-V70I8P242

[38] Ebrahimi, A., Ghorbani, B., Taghavi, M. "Novel integrated structure consisting of CO_2 capture cycle, heat pump unit, Kalina power, and ejector refrigeration systems for liquid CO_2 storage using renewable energies", Energy Science & Engineering, 10(8), pp. 3167–3188, 2022. https://doi.org/10.1002/ese3.1211

[39] Ghorbani, B., Salehi, G., Ebrahimi, A., Taghavi, M. "Energy, exergy and pinch analyses of a novel energy storage structure using post-combustion CO_2 separation unit, dual pressure Linde–Hampson liquefaction system, two-stage organic Rankine cycle and geothermal energy", Energy, 233, 121051, 2021. https://doi.org/10.1016/j.energy.2021.121051

[40] Afrouzy, Z. A., Taghavi, M. "Thermo-economic analysis of a novel integrated structure for liquefied natural gas production using photovoltaic panels", Journal of Thermal Analysis and Calorimetry, 145(3), pp. 1509–1536, 2021. https://doi.org/10.1007/s10973-021-10769-4

[41] Tran, F., Blaha, P. "Accurate Band Gaps of Semiconductors and Insulators with a Semilocal Exchange-Correlation Potential", Physical Review Letters, 102(22), 226401, 2009. https://doi.org/10.1103/PhysRevLett.102.226401

[42] Monkhorst, H. J., Pack, J. D. "Special points for Brillouin-zone integrations", Physical Review B, 13(12), pp. 5188–5192, 1976. https://doi.org/10.1103/PhysRevB.13.5188

[43] Zhang, X., Li, T., Hu, C., Fu, Z., Lin, J., Cheng, Z., Wu, J., Qi, Y., Ruan, Y., Huang, L. "Investigation of efficient all-inorganic HTL-free $CsGeI_3$ perovskite solar cells by device simulation", Materials Today Communications, 34, 105347, 2023. https://doi.org/10.1016/j.mtcomm.2023.105347

[44] Ijaz, S., Raza, E., Ahmad, Z., Zubair, M., Mehmood, M. Q., Mehmood, H., Massoud, Y., Rehman, M. M. "Numerical simulation to optimize the efficiency of HTM-free perovskite solar cells by ETM engineering", Solar Energy, 250, pp. 108–118, 2023. https://doi.org/10.1016/j.solener.2022.12.027

[45] Mushtaq, S., Tahir, S., Ashfaq, A., Bonilla, R. S., Haneef, M., Saeed, R., Ahmad, W., Amin, N. "Performance optimization of lead-free $MASnBr_3$ based perovskite solar cells by SCAPS-1D device simulation", Solar Energy, 249, pp. 401–413, 2023. https://doi.org/10.1016/j.solener.2022.11.050

[46] Qiao, Z., Zhang, M., Wu, B., Zhang, T., Ruan, Y., Chen, J., Huang, L., Wu, J., Qi, Y., Yang, X. "Inorganic tin-based perovskite solar cells: Modeling and performance analysis of hole-transport-layer-free structures", Chemical Physics Letters, 813, 140295, 2023. https://doi.org/10.1016/j.cplett.2022.140295

[47] Haneef, M., Tahir, S., Mahmoud, H. A., Ali, A., Ashfaq, A. "Optimizing Lead-free $MASnBr_3$ Perovskite Solar Cells for High-Efficiency and Long-Term Stability Using Graphene and Advanced Interface Layers", ACS Omega, 9(6), pp. 7053–7060, 2024. https://doi.org/10.1021/acsomega.3c08981

[48] Rai, N., Rai, S., Singh, P. K., Lohia, P., Dwivedi, D. K. "Analysis of various ETL materials for an efficient perovskite solar cell by numerical simulation", Journal of Materials Science: Materials in Electronics, 31(19), pp. 16269–16280, 2020. https://doi.org/10.1007/s10854-020-04175-z

[49] Khan, Z., Noman, M., Jan, S. T., Khan, A. D. "Systematic investigation of the impact of kesterite and zinc based charge transport layers on the device performance and optoelectronic properties of ecofriendly tin (Sn) based perovskite solar cells", Solar Energy, 257, pp. 58–87, 2023. https://doi.org/10.1016/j.solener.2023.04.019

[50] Adjouz, R., Allam, Z., Souli, L., H. L., Hafaifa, L., Zebeir, A. "Simulation and modeling of a new $CsSnI_3$ solar cell structure: A numerical study", Semiconductor Science and Technology, 39(12), 125010, 2024. https://doi.org/10.1088/1361-6641/ad8ae2

[51] Bag, A., Radhakrishnan, R., Nekovei, R., Jeyakumar, R. "Effect of absorber layer, hole transport layer thicknesses, and its doping density on the performance of perovskite solar cells by device simulation", Solar Energy, 196, pp. 177–182, 2020. https://doi.org/10.1016/j.solener.2019.12.014

[52] Samanta, M., Ahmed, S. I., Chattopadhyay, K. K., Bose, C. "Role of various transport layer and electrode materials in enhancing performance of stable environment-friendly Cs_2TiBr_6 solar cell", Optik, 217, 164805, 2020. https://doi.org/10.1016/j.ijleo.2020.164805

[53] Jan, S. T., Noman, M. "Influence of layer thickness, defect density, doping concentration, interface defects, work function, working temperature and reflecting coating on lead-free perovskite solar cell", Solar Energy, 237, pp. 29–43, 2022. https://doi.org/10.1016/j.solener.2022.03.069

[54] Dris, K., Benhaliliba, M. "Novel inorganic–organic heterojunction solar cell-based perovskite using two absorbent materials", Nano, 18(11), 2350091, 2023. https://doi.org/10.1142/S1793292023500911

[55] Ahmed, S., Jannat, F., Khan, M. A. K., Alim, M. A. "Numerical development of eco-friendly Cs_2TiBr_6-based perovskite solar cell with all-inorganic charge transport materials via SCAPS-1D", Optik, 225, 165765, 2021. https://doi.org/10.1016/j.ijleo.2020.165765

[56] Anwar, F., Mahbub, R., Satter, S. S., Ullah, S. M. "Effect of different HTM layers and electrical parameters on ZnO nanorod-based lead-free perovskite solar cell for high-efficiency performance", International Journal of Photoenergy, 2017. https://doi.org/10.1155/2017/9846310

[57] Mohanty, I., Mangal, S., Singh, U. P. "Performance optimization of lead-free $MASnI_3$/CIGS heterojunction solar cell with 28.7% efficiency: A numerical approach", Optical Materials, 122, 111812, 2021. https://doi.org/10.1016/j.optmat.2021.111812

[58] Dris, K., Shafeera, N. N., Benhaliliba, M., Ahmed, A. B. E. N., Bouandas, H., Kumar, R., Ayeshamariam, A. "Using SCAPS to simulate solar cells by obtaining data for perovskites from DFT", Bulletin of Materials Science, 48(4), 120, 2025. https://doi.org/10.1007/s12034-025-03486-3

[59] Jayan, D. K., Sebastian, V., Kurian, J. "Simulation and optimization studies on $CsPbI_3$-based inorganic perovskite solar cells", Solar Energy, 221, pp. 99–108, 2021.
https://doi.org/10.1016/j.solener.2021.04.030

[60] Park, H. J., Son, H., Jeong, B. S. "SCAPS-1D simulation for device optimization to improve efficiency in lead-free $CsSnI_3$ perovskite solar cells", Inorganics, 12(4), 123, 2024.
https://doi.org/10.3390/inorganics12040123

[61] Dris, K., Benhaliliba, M. "Novel inorganic–organic heterojunction solar cell based on Pt/$CuSbS_2$/Abs/ZnO/FTO perovskite using two MAPI and FAPI absorbent materials", Algerian Journal of Research in Technology, 8(1), pp. 42–56, 2024.
https://doi.org/10.58681/ajrt.24080105

[62] Ashfaq, A., Tahir, S., Mushtaq, S., Alqurashi, R. S., Haneef, M., Almousa, N., Rehman, U., Bonilla, R. S. "Comparative performance analysis of Cs_2TiX_6 ($X = Br^-, Cl^-, I^-$) lead-free perovskite solar cells incorporating single, double and triple layer halides by SCAPS-1D", Materials Today Communications, 35, 106016, 2023.
https://doi.org/10.1016/j.mtcomm.2023.106016

[63] Yousuf, R., Qazi, G. "Numerical modelling: Design and investigation of uniformly and non-uniformly doped absorber layer-based PN homojunction perovskite solar cell variants", Solar Energy, 228, pp. 427–438, 2021.
https://doi.org/10.1016/j.solener.2021.09.079

[64] Al-Reyahi, A. Y., Mufleh, A., Al Azar, S. M., Maghrabi, M., Al Aqtash, N., Essaoud, S. S., Berarma, K., Shaheen, A., Ketfi, M. E., Mousa, A. A. "Exploring the physical properties of cubic $CsGeBr_{3-n}I_n$ (n = 0, 1, 2, 3) compounds: Ab initio calculations of perovskites prospective for solar cell applications", Solid State Sciences, 148, 107435, 2024.
https://doi.org/10.1016/j.solidstatesciences.2023.107435

[65] Ali, H., Haque, D., Hossain, M., Zafor, A., Islam, T. "Improving the efficiency of ZnTe-based heterojunction solar cell with In_2Te_3 BSF layer", Journal of Applied Electrochemistry, 54(5), pp. 1013–1031, 2023.
https://doi.org/10.1007/s10800-023-02013-8

[66] Dris, K., Benhaliliba, M. "Study and optimization of a new perovskite solar cell structure based on two absorber materials Cs_2TiBr_6 and $MASnBr_3$ using SCAPS-1D", Periodica Polytechnica Chemical Engineering, 68(3), pp. 348–363, 2024.
https://doi.org/10.3311/PPch.36825

[67] Dris, K., Benhaliliba, M., Ayeshamariam, A., Roy, A., Kaviyarasu, K. "Improving the perovskite solar cell by insertion of methylammonium tin oxide and cesium tin chloride as absorber layers: SCAPS-1D study based on experimental studies", Journal of Optics, 54(5), pp. 3387–3409, 2025.
https://doi.org/10.1007/s12596-024-01996-7

[68] Jamal, M., Asadabadi, S. J., Ahmad, I., Aliabad, H. A. R. "Elastic constants of cubic crystals", Computational Materials Science, 95, pp. 592–599, 2014.
https://doi.org/10.1016/j.commatsci.2014.08.027

[69] Mitra, S., Pak, Y., Alaal, N., Hedhili, M. N., Almalawi, D. R., Alwadai, N., Loganathan, K., Kumarasan, Y., Lim, N., Jung, G. Y., Roqan, I. S. "Novel P-Type Wide Bandgap Manganese Oxide Quantum Dots Operating at Deep UV Range for Optoelectronic Devices", Advanced Optical Materials, 7(21), 1900801, 2019.
https://doi.org/10.1002/adom.201900801

[70] Li, X., Zhao, J., Xu, J. "Mechanical properties of bcc Fe-Cr alloys by first-principles simulations", Frontiers in Physics, 7(3), pp. 360–365, 2012.
https://doi.org/10.1007/s11467-011-0193-0

[71] Hilal, M., Rashid, B., Khan, S. H., Khan, A. "Investigation of electro-optical properties of InSb under the influence of spin-orbit interaction at room temperature", Materials Chemistry and Physics, 184, pp. 41–48, 2016.
https://doi.org/10.1016/j.matchemphys.2016.09.009

[72] Islam, M. N., Podder, J., Ali, M. L. "The effect of metal substitution in $CsSnI_3$ perovskites with enhanced optoelectronic and photovoltaic properties", RSC Advances, 11(62), pp. 39553–39563, 2021.
https://doi.org/10.1039/D1RA07609D

[73] Greaves, G. N., Greer, A. L., Lakes, R. S., Rouxel, T. "Poisson's ratio and modern materials", Nature Materials, 10(11), pp. 823–837, 2011.
https://doi.org/10.1038/nmat3134

[74] Dar, S. A., Srivastava, V., Sakalle, U. K., Parey, V. "Electronic structure, magnetic, mechanical and thermo-physical behavior of double perovskite Ba_2MgOsO_6", European Physical Journal Plus, 133(2), 64, 2018.
https://doi.org/10.1140/epjp/i2018-11889-y

[75] Thiele, G., Rotter, H. W., Schmidt, K. D. "Kristallstrukturen und Phasentransformationen von Caesiumtrihalogenogermanaten(II) $CsGeX_3$ (X = Cl, Br, I)" (Crystal structures and phase transformations of caesium trihalogenogermanates(II) $CsGeX_3$ (X = Cl, Br, I)), Zeitschrift für Anorganische und Allgemeine Chemie, 545(2), pp. 148–156, 1987. (in German)
https://doi.org/10.1002/zaac.19875450217

[76] Shakil, M., Akram, A., Zeba, I., Ahmad, R., Gillani, S. S. A., Gadhi, M. A. "Effect of mixed halide contents on structural, electronic, optical and elastic properties of $CsSnI_{3-x}Br_x$ for solar cell applications: first-principles study", Materials Research Express, 7(2), 25513, 2020.
https://doi.org/10.1088/2053-1591/ab727d

[77] Yamada, K., Funabiki, S., Horimoto, H., Matsui, T., Okuda, T., Ichiba, S. "Structural Phase Transitions of the Polymorphs of $CsSnI_3$ by Means of Rietveld Analysis of the X-Ray Diffraction", Chemical Letters, 20(5), pp. 801–804, 2006.
https://doi.org/10.1246/cl.1991.801

[78] Houari, M., Bouadjemi, B., Matougui, M., Haid, S., Lantri, T., Aziz, Z., Bentata, S., Bouhafs, B. "Optoelectronic properties of germanium iodide perovskites $AGeI_3$ (A = K, Rb, Cs): first principles investigations", Optical and Quantum Electronics, 51(7), 234, 2019.
https://doi.org/10.1007/s11082-019-1949-y

[79] Stoumpos, C. C., Frazer, L., Clark, D. J., Kim, Y. S., Rhim, S. H., Freeman, A. J., Ketterson, J. B., Jang, J. I., Kanatzidis, M. G. "Hybrid Germanium Iodide Perovskite Semiconductors: Active Lone Pairs, Structural Distortions, Direct and Indirect Energy Gaps, and Strong Nonlinear Optical Properties", Journal of the American Chemical Society, 137(21), pp. 6804–6819, 2015.
https://doi.org/10.1021/jacs.5b01025

[80] Sabba, D., Mulmudi, H. K., Prabhakar, R. R., Krishnamoorthy, T., Baikie, T., Boix, P. P., Mhaisalkar, S., Mathews, N. "Impact of Anionic Br^- Substitution on Open Circuit Voltage in Lead-Free Perovskite ($CsSnI_{3-x}Br_x$) Solar Cells", Journal of Physical Chemistry C, 119(4), pp. 1763–1767, 2015.
https://doi.org/10.1021/jp5126624

[81] Bardeen, J., Shockley, W. "Deformation Potentials and Mobilities in Non-Polar Crystals", Physical Review, 80(1), pp. 72–80, 1950. https://doi.org/10.1103/PhysRev.80.72

[82] Hill, R. "The Elastic Behaviour of a Crystalline Aggregate", Proceedings of the Physical Society. Section A, 65(5), 349, 1952. https://doi.org/10.1088/0370-1298/65/5/307

[83] Husain, M., Rahman, N., Azzouz-Rached, A., Sfina, N., Asad, M., …, Alosaimi, G. "Investigating structural, optoelectronic, and mechanical properties of novel Tungsten-based oxides double-perovskites compounds Sr_2XWO_6 (X = Mn, Fe): A DFT approach", Optik, 315, 172045, 2024. https://doi.org/10.1016/j.ijleo.2024.172045

[84] Behera, D., Geleta, T. A., Allaoui, I., Khuili, M., Mukherjee, S. K., Akila, B., Al-Qaisi, S. "First-principle analysis of optical and thermoelectric properties in alkaline-based perovskite compounds $AInCl_3$ (A = K, Rb)", European Physical Journal Plus, 139(2), 127, 2024. https://doi.org/10.1140/epjp/s13360-024-04921-w

[85] Liu, H., Zhang, H. "Structural, Electronic and Optical Properties of $CsMI_3$ (M = Ge, Sn, Pb) Perovskite from First Principles", American Scientific Research Journal for Engineering, Technology, and Sciences, 71(1), pp. 87–98, 2020

[86] Tang, L.-C., Chang, Y.-C., Huang, J.-Y., Lee, M.-H., Chang, C.-S. "First Principles Calculations of Linear and Second-Order Optical Responses in Rhombohedrally Distorted Perovskite Ternary Halides, $CsGeX_3$ (X = Cl, Br, I)", Japanese Journal of Applied Physics, 48(11), 112402, 2009. https://doi.org/10.1143/JJAP.48.112402

[87] Belhachi, S., Al-Qaisi, S., Samah, S., Rached, H., Zaman, A., Alrebdi, T. A., Boutramine, A., Erum, N., Ahmed, R., Verma, A. S. "DFT Analysis of Ba_2NbRhO_6: A Promising Double Perovskite for Sustainable Energy Applications", Journal of Inorganic and Organometallic Polymers and Materials, 35(2), pp. 978–993, 2025. https://doi.org/10.1007/s10904-024-03336-5

[88] Heyd, J., Peralta, J. E., Scuseria, G. E., Martin, R. L. "Energy band gaps and lattice parameters evaluated with the Heyd-Scuseria-Ernzerhof screened hybrid functional", Journal of Chemical Physics, 123(17), 174101, 2005. https://doi.org/10.1063/1.2085170

[89] Dufek, P., Blaha, P., Schwarz, K. "Applications of Engel and Vosko's generalized gradient approximation in solids", Physical Review B, 50(11), pp. 7279–7283, 1994. https://doi.org/10.1103/PhysRevB.50.7279

[90] Körbel, S., Marques, M. A. L., Botti, S. "Stability and electronic properties of new inorganic perovskites from high-throughput ab initio calculations", Journal of Materials Chemistry C, 4(15), pp. 3157–3167, 2016. https://doi.org/10.1039/C5TC04172D

[91] Rahman, N., Husain, M., Azzouz-Rached, A., Al-Ammar, E. A., Sfina, N., …, Rashid, A. U. "Theoretical investigations of double perovskites Rb_2YCuX_6 (X = Cl, F) for green energy applications: DFT study", Journal of Physics and Chemistry of Solids, 193, 112171, 2024. https://doi.org/10.1016/j.jpcs.2024.112171

[92] Belhachi, S. "First-principles prediction of structural, electronic, magnetic and optical properties of ErN and TmN in the hexagonal structure", Optik, 262, 169226, 2022. https://doi.org/10.1016/j.ijleo.2022.169226

[93] Al-Qaisi, S., Rached, H., Alrebdi, T. A., Bouzgarrou, S., Behera, D., Mukherjee, S. K., Khuili, M., Adam, M., Verma, A. S., Ezzeldien, M. "Study of mechanical, optical, and thermoelectric characteristics of Ba_2XMoO_6 (X = Zn, Cd) double perovskite for energy harvesting", Journal of Computational Chemistry, 44(32), pp. 2442–2452, 2023. https://doi.org/10.1002/jcc.27209

[94] Belhachi, S., Kanoun, M. B., Goumri-Said, S. "Unveiling the potential of $CuAl_xGa_{1-x}Se_2$ (x = 0.25) chalcopyrite as absorbent for photovoltaic application: first-principles insights into the structural, elastic, mechanical, electronic, thermodynamic and optical properties", Physica Scripta, 99(8), 85921, 2024. https://doi.org/10.1088/1402-4896/ad5b93

[95] Riaz, K., Drissi, N., Abdalla, S., Belhachi, S., Bousbih, R., Soliman, M. S., Nasarullah, Hasanin, T. H. A., Nazar, M., Ali Abdulhussein, N. "Computational Exploration of Structural, Elastic, Optoelectronic and Magnetic Properties of A_2YHgCl_6 (A = Cs, K) Using Enhanced Computational Techniques", Journal of Inorganic and Organometallic Polymers and Materials, 35(7), pp. 5363–5376, 2025. https://doi.org/10.1007/s10904-025-03594-x

[96] Akhtar, M., Alanazi, F. K., Sajid, M., Abdalla, S., Belhachi, S., …, Ahmad, M. S. "Investigating the Physical Characteristics of Halide Double Perovskites X_2LiSbI_6 (X = K, Cs): A First-Principles Approach", Journal of Inorganic and Organometallic Polymers and Materials, 35(6), pp. 4810–4824, 2025. https://doi.org/10.1007/s10904-024-03560-z

[97] Saidi, S., Belhachi, S., Abdalla, S., Al-Humaidi, J. Y., Iqbal, M. W., Al-Saleem, M. S. M., Rahman, M. M., Sillanpää, M., Kumar, A., Singh, S. "K_2AlInZ_6 (Z = F, Cl, Br) Double Perovskites: Potential Candidates for Optoelectronic and Photovoltaic Devices", Journal of Computational Chemistry, 46(25), e70222, 2025. https://doi.org/10.1002/jcc.70222

[98] Rahman, N., Husain, M., Ahmad, Y., Azzouz-Rached, A., Al-khamiseh, B. M., …, Uzair, M. "First-principles investigation of Cs_2TlGaX_6 (X = Cl, F) double perovskites: structural and dynamical stability, elastic properties, and optoelectronic characteristics for applications in semiconductor technology", Optical and Quantum Electronics, 56(8), 1298, 2024. https://doi.org/10.1007/s11082-024-07199-5

[99] Hasan, N., Arifuzzaman, M., Kabir, A. "Structural, elastic and optoelectronic properties of inorganic cubic $FrBX_3$ (B = Ge, Sn; X = Cl, Br, I) perovskite: the density functional theory approach", RSC Advances, 12(13), pp. 7961–7972, 2022. https://doi.org/10.1039/d2ra00546h

[100] Belhachi, S., Samah, S., Abdalla, S., Iqbal, M. W., Al-Humaidi, J. Y., Batterjee, M. G., Rahman, M. M. "Comprehensive exploration of rare-earth chalcogenides: A DFT-based investigation into their optoelectronic, elastic, thermomechanical and magnetic properties for advanced functional and high-temperature applications", Inorganic Chemistry Communications, 177, 114442, 2025. https://doi.org/10.1016/j.inoche.2025.114442